Monthly Notices of the ROYAL ASTRONOMICAL SOCIETY

MNRAS **516,** 138–157 (2022) https://doi.org/10.1093/mnras/stac2238
Advance Access publication 2022 August 11

Probing the $z \gtrsim 6$ quasars in a universe with IllustrisTNG physics: impact of gas-based black hole seeding models

Aklant K. Bhowmick [1]★ Laura Blecha,[1] Yueying Ni,[2,3] Tiziana Di Matteo,[2,3] Paul Torrey [1] Luke Zoltan Kelley [4] Mark Vogelsberger [5] Rainer Weinberger [6] and Lars Hernquist[7]

[1]*Department of Physics, University of Florida, Gainesville, FL 32611, USA*
[2]*McWilliams Center for Cosmology, 5000 Forbes Avenue, Pittsburgh, PA 15213, USA*
[3]*NSF AI Planning Institute for Physics of the Future, Carnegie Mellon University, Pittsburgh, PA 15213, USA*
[4]*Center for Interdisciplinary Exploration and Research in Astrophysics, Northwestern University, Evanston, IL 60208, USA*
[5]*Department of Physics, Kavli Institute for Astrophysics and Space Research, Massachusetts Institute of Technology, Cambridge, MA 02139, USA*
[6]*Canadian Institute for Theoretical Astrophysics, 60 St George Street, Toronto, ON M5S 3H8, Canada*
[7]*Harvard-Smithsonian Center for Astrophysics, 60 Garden Street, Cambridge, MA 02138, USA*

Accepted 2022 August 3. Received 2022 August 3; in original form 2022 May 9

ABSTRACT

We explore implications of a range of black hole (BH) seeding prescriptions on the formation of the brightest $z \gtrsim 6$ quasars in cosmological hydrodynamic simulations. The underlying galaxy formation model is the same as in the `IllustrisTNG` simulations. Using constrained initial conditions, we study the growth of BHs in rare overdense regions (forming $\gtrsim 10^{12}\,\mathrm{M}_\odot\,h^{-1}$ haloes by $z = 7$) using a $(9\ \mathrm{Mpc}\,h^{-1})^3$ simulated volume. BH growth is maximal within haloes that are compact and have a low tidal field. For these haloes, we consider an array of gas-based seeding prescriptions wherein $M_{\rm seed} = 10^4$–$10^6\,\mathrm{M}_\odot\,h^{-1}$ seeds are inserted in haloes above critical thresholds for halo mass and dense, metal-poor gas mass (defined as $\tilde{M}_{\rm h}$ and $\tilde{M}_{\rm sf,mp}$, respectively, in units of $M_{\rm seed}$). We find that a seed model with $\tilde{M}_{\rm sf,mp} = 5$ and $\tilde{M}_{\rm h} = 3000$ successfully produces a $z \sim 6$ quasar with $\sim 10^9\,\mathrm{M}_\odot$ mass and $\sim 10^{47}$ erg s^{-1} luminosity. BH mergers play a crucial role at $z \gtrsim 9$, causing an early boost in BH mass at a time when accretion-driven BH growth is negligible. With more stringent seeding conditions (e.g. $\tilde{M}_{\rm sf,mp} = 1000$), the relative paucity of BH seeds results in a much lower merger rate. In this case, $z \gtrsim 6$ quasars can only be formed if we enhance the maximum allowed BH accretion rates (by factors $\gtrsim$10) compared to the accretion model used in `IllustrisTNG`. This can be achieved either by allowing for super-Eddington accretion, or by reducing the radiative efficiency. Our results demonstrate that progenitors of $z \sim 6$ quasars have distinct BH merger histories for different seeding models, which will be distinguishable with Laser Interferometer Space Antenna observations.

Key words: methods: numerical – Galaxy: evolution – Galaxy: formation; (galaxies:) quasars: general; (galaxies:) quasars: supermassive black holes.

1 INTRODUCTION

The growing population of known luminous ($\sim 10^{47}$ erg s^{-1}) quasars at the highest redshifts ($z \gtrsim 6$) shows that some supermassive black holes (SMBHs) were already in place within the first $\sim$1 Gyr since the big bang. The inferred masses of these quasars lie in the range $\sim 10^9$–$10^{10}\,\mathrm{M}_\odot$, similar to the most massive SMBHs in the local universe. To date, $\gtrsim$200 quasars have already been discovered at $z \gtrsim 6$ (Fan et al. 2001; Willott et al. 2010; Venemans et al. 2015; Bañados et al. 2016; Jiang et al. 2016; Reed et al. 2017; Matsuoka et al. 2018), which overall correspond to number densities of comoving 1 Gpc^{-3} (hereafter, distances and volumes will be expressed in comoving units unless stated otherwise). Additionally, there are a handful of objects discovered at $z \gtrsim 7$ (Mortlock et al. 2011; Wang et al. 2018; Matsuoka et al. 2019; Yang et al. 2019), which includes the most distant quasars observed to date (Bañados et al. 2018; Wang et al. 2021) at $z \sim 7.6$. The recently launched *James Webb Space Telescope* (*JWST*; Gardner et al. 2006) and planned facilities such as Lynx X-ray Observatory (The Lynx Team 2018) have a promising prospect of revealing the active galactic nuclei (AGNs) progenitors of these quasars at even higher redshifts. Additionally, gravitational wave events from Laser Interferometer Space Antenna (LISA; Baker et al. 2019) will also provide insights into the prevalence of black hole (BH) mergers and the growth history of these quasars. These observations are going to be crucial to understanding the assembly of these quasars, which is an outstanding challenge for theoretical models of BH formation and growth.

The origin of these $z \gtrsim 6$ quasars, and the larger SMBH populations in general, is a subject of active debate. Remnants of the first generation of Pop III stars, a.k.a Pop III BH seeds, are popular candidates (Fryer, Woosley & Heger 2001; Madau & Rees 2001; Xu, Wise & Norman 2013; Smith et al. 2018). The BH seed mass that results from the conjectured Pop III scenario depends on the initial mass function of Pop III stars themselves. This is predicted to be more top heavy than present-day stellar populations, with masses typically in the range $\sim$ 10–100 $\mathrm{M}_\odot$ (Hirano et al. 2014; Hosokawa et al. 2016). But even the most massive Pop III seeds (initial BH

★ E-mail: aklant.app@gmail.com

masses of $\sim 10^2\,M_\odot$) would require significant periods of super-Eddington accretion to grow by $\gtrsim$7 orders of magnitude to form a $z \gtrsim 6$ quasar. These stringent growth rate requirements can be alleviated to an extent with channels producing more massive seeds. Theories proposed for massive seed formation include runaway collisions of stars or BHs in dense nuclear star clusters forming 'NSC seeds' with masses $\sim 10^2$–$10^3\,M_\odot$ (Davies, Miller & Bellovary 2011; Lupi et al. 2014; Kroupa et al. 2020; Das et al. 2021b, a), and direct collapse of gas in atomic cooling ($T_{\rm vir} > 10^4$ K) haloes forming 'direct collapse black hole (DCBH) seeds' with masses $\sim 10^4$–$10^6\,M_\odot$ (Bromm & Loeb 2003; Begelman, Volonteri & Rees 2006; Regan, Johansson & Wise 2014; Latif, Schleicher & Hartwig 2016; Luo et al. 2018; Wise et al. 2019; Luo et al. 2020).

The most massive DCBH seeds are seen as promising candidates for explaining the rapid formation of the $z \gtrsim 6$ quasars. DCBHs are also exciting because there is a potential for directly detecting them using *JWST* (Natarajan et al. 2017; Cann et al. 2018; Inayoshi et al. 2022). Their formation requires gas to undergo an isothermal collapse at temperatures $\gtrsim 10^4$ K (corresponding to a Jeans mass $\gtrsim 10^4\,M_\odot$). For this to occur, the gas needs to be devoid of chemical species that are efficient coolants at $\lesssim 10^4$ K, namely metals and molecular hydrogen. To suppress molecular hydrogen, the gas must be exposed to Lyman Werner radiation with minimum fluxes $\gtrsim 1000\,J_{21}$ as inferred from small-scale hydrodynamic simulations (Shang, Bryan & Haiman 2010) as well as one-zone chemistry models (Sugimura, Omukai & Inoue 2014; Wolcott-Green, Haiman & Bryan 2017). Such high fluxes can only be provided by nearby star-forming galaxies (Visbal, Haiman & Bryan 2014; Regan et al. 2017; Bhowmick et al. 2021a; Lupi, Haiman & Volonteri 2021). However, these star-forming regions can also pollute the gas with metals, which would then eliminate any possibility of direct collapse. This implies that the window for DCBH seed formation is extremely narrow, especially if it requires the presence of such high LW fluxes. However, there may also be scenarios where DCBH formation could occur without the need for LW radiation. These include alternative mechanisms that can destroy H_2. For example, collisional dissociation of H_2 within hot ($\gtrsim 10^4$ K) and dense ($\gtrsim 10^3$ cm^{-3}) gas via the excitation of the rotovibrational levels (Inayoshi & Omukai 2012). Trapping of Lyman-α radiation in regions with high enough neutral Hydrogen column densities can also prevent H_2 formation (Spaans & Silk 2006; Schleicher, Spaans & Glover 2010; Latif, Zaroubi & Spaans 2011). In addition, even in the presence of H_2, supersonic baryonic streams in rare massive haloes can enhance the Jeans mass of the gas and promote the formation of DCBHs (Tanaka & Li 2014; Hirano et al. 2017; Schauer et al. 2019). Dynamical heating induced by rapid growth of massive haloes can also compete with H_2 cooling, and thereby promote DCBH formation at substantially lower LW fluxes ($\sim 3\,J_{21}$) (Fernandez et al. 2014; Wise et al. 2019; Regan et al. 2020). Very recently, Latif et al. (2022) found a new mechanism for forming DCBHs via catastrophic collapse of baryons in rare haloes where prior star formation is suppressed by supersonic turbulence generated by cold accretion flows. Despite these different possible scenarios under which DCBHs could potentially form, they all occur in the rarest regions in the early universe. It is therefore unclear whether they form abundantly enough to explain the inferred densities of these objects.

Semi-analytic models (SAMs) have so far been extensively used in the modelling of BH seeds (Sesana, Volonteri & Haardt 2007; Volonteri & Natarajan 2009; Barausse 2012; Ricarte & Natarajan 2018; Valiante et al. 2018; Dayal et al. 2019; DeGraf & Sijacki 2020). Several such SAMs have also been used to study the feasibility of different seeding channels as possible origins of $z \gtrsim 6$ quasars. For example, Valiante et al. (2011, 2012, 2014) developed the GAMETTE-QSODUST data constrained SAM to probe the $z \gtrsim 6$ quasars and their host galaxies. This model was used in Valiante et al. (2016) and Sassano et al. (2021), showing that the formation of heavy seeds ($\sim 10^5\,M_\odot$) is most crucial to the assembly of the first quasars, particularly in models where the BH accretion rate is capped at the Eddington limit. Pezzulli, Valiante & Schneider (2016) and Pezzulli et al. (2017) showed that light seeds ($\sim 10^2\,M_\odot$) require super-Eddington accretion to grow into the $z \gtrsim 6$ quasars. Lupi et al. (2021) applied a semi-analytic framework on a dark-matter-only simulation of a $3 \times 10^{12}\,M_\odot$ halo forming at $z = 6$ (presumably hosting a luminous quasar); they demonstrated that the progenitors of this halo can be sites for the formation of massive DCBH seeds. Li, Inayoshi & Qiu (2021) also performed a similar study but using a large ensemble (10^4 realizations) of merger trees of a $\sim 10^{12}\,M_\odot$ halo generated using Monte Carlo approach. They revealed a substantial influence of dynamical heating in halo mergers, as well as baryonic streaming, in promoting DCBH seed formation in the progenitors of high-z quasar hosts.

While SAMs, being computationally inexpensive, can probe a wide range of seed models relatively quickly, they are unable to self-consistently track the hydrodynamics of gas. Cosmological hydrodynamic simulations (Di Matteo et al. 2012; Vogelsberger et al. 2014b; Khandai et al. 2015; Schaye et al. 2015; Sijacki et al. 2015; Dubois et al. 2016; Volonteri et al. 2016; Kaviraj et al. 2017; Tremmel et al. 2017; Nelson et al. 2019; Volonteri et al. 2020) are more readily able to decipher the role of gas hydrodynamics in forming the $z \gtrsim 6$ quasars (see e.g. the review by Vogelsberger et al. 2020a). Since the $z \gtrsim 6$ quasars are extremely rare, we need extremely large volumes to probe these objects (note however that they are much more computationally expensive than SAMs). MassiveBlack (Di Matteo et al. 2012), with a volume of $[0.75\,{\rm Gpc}]^3$, revealed that $z \gtrsim 6$ quasars can form in extremely massive haloes ($\gtrsim 10^{12}\,M_\odot\,h^{-1}$ at $z \sim 6$) via a steady inflow of cold gas driving sustained accretion rates close to the Eddington limit. This was further confirmed using follow-up zoom simulations at much higher resolutions (Feng et al. 2014). BlueTides (Feng et al. 2016), with a volume of $[0.5\,{\rm Gpc}]^3$ (but higher resolution compared to MassiveBlack), further revealed the role of higher order features (particularly low tidal fields, see Di Matteo et al. 2017) of the initial density field in producing the fastest accretion rates necessary to assemble the $z \gtrsim 7$ quasars.

The results of Di Matteo et al. (2017) motivated Ni, Matteo & Feng (2021) (hereafter N21), which was a systematic study of the impact of higher order features of rare density peaks on the subsequent BH growth. Using the method of constrained Gaussian realizations (Hoffman & Ribak 1991; van de Weygaert & Bertschinger 1996), N21 was able to generate initial conditions comprising of the rarest density peaks with the desired higher order features (i.e. first- and second-order derivatives). They demonstrated that highly compact peaks with low tidal fields led to the fastest BH growth. Due to their finite resolution however, cosmological hydrodynamic simulations are limited in terms of their ability to probe low-mass BH seeding channels. Consequently, the vast majority of the simulations targeting $z \gtrsim 6$ quasars described in the previous paragraph (also including Sijacki, Springel & Haehnelt 2009; Costa et al. 2014; Curtis & Sijacki 2016; Zhu et al. 2020) used simple halo-based seeding prescriptions (seeds are inserted in haloes above a prescribed halo mass) that do not distinguish between different physical seeding channels. Therefore, while all these simulations have been generally successful in broadly reproducing the $z \gtrsim 6$ quasars, their ability to reveal insights into the seeding environments of these objects is still limited. With upcoming LISA measurements being amongst

the most promising probes for revealing the mechanism of BH seed formation, the time is ripe for developing simulations that can reliably distinguish between different BH seeding channels.

Numerous studies have implemented gas-based BH seeding prescriptions (Bellovary et al. 2011; Dubois et al. 2013; Hirschmann et al. 2014; Taylor & Kobayashi 2015; Volonteri et al. 2016; Habouzit, Volonteri & Dubois 2017; Kaviraj et al. 2017; Tremmel et al. 2017; Davé et al. 2019; Trebitsch et al. 2020; Lee et al. 2021). Bhowmick et al. (2021a, b) have recently conducted a systematic study to assess the impact of gas-based BH seeding prescriptions on $z \gtrsim 7$ SMBH populations. These seed models are built on the framework of the IllustrisTNG galaxy formation model (Weinberger et al. 2017; Pillepich et al. 2018a). They seeded BHs in haloes via criteria based on dense, metal-poor gas mass, halo mass, gas spin as well as incident Lyman Werner (LW) flux. The resulting family of models is generally agnostic about which theoretical seeding channels they represent, but their parameters could be tuned to represent any of the seeding channels described above (PopIII, NSC, or DCBH). By applying these models to zoom simulations of modestly overdense regions (3.3σ overdensity, targeting a $\sim 10^{11}\,\mathrm{M}_\odot\,h^{-1}$ halo at $z = 5$), they found that changing different seed parameters would leave qualitatively distinct imprints on the BH merger rates. In particular, Bhowmick et al. (2021b) found that when the dense, metal-poor gas mass threshold is increased, it suppresses the seeding and merger rates more strongly at $z \lesssim 15$ compared to higher redshifts. On the other hand, an increase in the total halo mass threshold for seeding causes stronger suppression of seeding and merger rates at $z \sim 11$–25 compared to $z \lesssim 11$. These results suggest that discrepancies between the merger rates of LISA binaries will contain insights into their seeding environments. Bhowmick et al. (2021a) found that even when a moderately low LW flux threshold ($\gtrsim 50\,J_{21}$) is adopted for seeding, it can dramatically suppress seed formation and prevent the assembly of $z \gtrsim 7$ SMBHs. This suggests that the bulk of the $z \gtrsim 7$ SMBH population (likely revealed by *JWST* and Lynx) may not originate from DCBH seeding channels.

The zoom regions of Bhowmick et al. (2021a, b) were not nearly overdense enough to be possible sites for the formation of $z \gtrsim 6$ quasars. In this work, we use constrained Gaussian realizations of extreme overdense regions ($\gtrsim 5\sigma$ overdensities forming $\gtrsim 10^{12}\,\mathrm{M}_\odot\,h^{-1}$ haloes by $z \sim 7$), and investigate the impact of BH seed models on the formation of the $z \gtrsim 6$ quasars. Apart from the seed models, our underlying galaxy formation model is adopted from the IllustrisTNG simulation suite.

Section 2 describes the simulation set-up, including the main features of the IllustrisTNG galaxy formation model, the BH seeding and accretion models, and the generation of the constrained initial conditions. Section 3 describes the main results concerning the impact of environment, seeding, and accretion models on BH growth. Finally, Section 4 summarizes the main conclusions of our work.

2 SIMULATION SET-UP

Our simulations were run using the AREPO code (Springel 2010; Pakmor, Bauer & Springel 2011; Pakmor et al. 2016; Weinberger, Springel & Pakmor 2020), which includes a gravity and magneto-hydrodynamics (MHD) solver. The simulations are cosmological in nature, which are performed within a representative portion of an expanding universe described by a fixed comoving volume (9 cMpc h^{-1} box size) with the following cosmology adopted from Planck Collaboration XIII (2016): ($\Omega_\Lambda = 0.6911$, $\Omega_\mathrm{m} = 0.3089$, $\Omega_b = 0.0486$, $H_0 = 67.74$ km s^{-1} Mpc^{-1}, $\sigma_8 = 0.8159$, $n_s = 0.9667$). The code uses a PM-Tree (Barnes & Hut 1986) method to solve for gravity, which is contributed by dark matter, gas, stars, and BHs. Within the resulting gravitational potential, the gas dynamics is computed by the MHD solver, which uses a quasi-Lagrangian description of the fluid within an unstructured grid generated via a Voronoi tessellation of the domain.

Our galaxy formation model is adopted from the IllustrisTNG simulation suite (Marinacci et al. 2018; Naiman et al. 2018; Nelson et al. 2018; Pillepich et al. 2018b; Springel et al. 2018; Nelson et al. 2019) (see also also Genel et al. 2018; Weinberger et al. 2018; Donnari et al. 2019; Pillepich et al. 2019; Rodriguez-Gomez et al. 2019; Torrey et al. 2019; Habouzit et al. 2021; Übler et al. 2021). The only substantive changes to the galaxy formation implemented here are in the sub-grid prescriptions for BH seeding and accretion. The remaining aspects of our galaxy formation model are the same as IllustrisTNG, which are detailed in Weinberger et al. (2017) and Pillepich et al. (2018a); here, we provide a brief summary:

(i) Energy loss via radiative cooling includes contributions from primordial species (H, H^+, He, He^+, He^{++}, based on Katz, Weinberg & Hernquist 1996), as well as metals (using pre-calculated tables for cooling rates as in Smith, Sigurdsson & Abel 2008) in the presence of a spatially uniform, time-dependent UV background. Note that cooling due to molecular Hydrogen (H_2) is not explicitly included in the model.

(ii) Stars are stochastically formed within gas cells with densities exceeding 0.1 cm^{-3} with an associated time-scale of 2.2 Gyr. The star-forming gas cells then represent an unresolved multiphase interstellar medium, which is modelled by an effective equation of state (Springel & Hernquist 2003; Vogelsberger et al. 2014a). The model implicitly assumes that stars are produced within an unresolved cold dense component in these gas cells, which would presumably form via H_2 cooling.

(iii) The stellar evolution model is adopted from Vogelsberger et al. (2013) with modifications for IllustrisTNG as in Pillepich et al. (2018a). Star particles represent a single stellar population with fixed age and metallicity. The initial mass function is assumed to be Chabrier (2003). The stellar evolution subsequently leads to chemical enrichment, wherein the evolution of seven species of metals (C, N, O, Ne, Mg, Si, Fe) are individually tracked in addition to H and He. Note here that prior to enrichment caused by stellar evolution, the gas is assigned an initial metallicity of $7 \times 10^{-8}\,Z_\odot$.

(iv) Feedback from stars and Type Ia/II Supernovae are modelled as galactic scale winds (Pillepich et al. 2018b), via which mass, momentum, and metals are deposited on to the gas surrounding the star particles.

(v) Models for BH formation and growth are detailed in the next two subsections. The treatment of BH dynamics and mergers is the same as in IllustrisTNG. Due to the limited gas mass resolution, our simulations cannot self-consistently reveal the small-scale dynamics of BHs, particularly at their lowest masses. To stabilize the BH dynamics, they are 'repositioned' to the nearest potential minimum within its 'neighbourhood' (defined by 10^3 nearest neighbouring gas cells). As a result, a BH is also promptly merged when it is within the neighbourhood of another BH.

2.1 BH seeding

We consider a range of BH seeding prescriptions, which include the default halo-based seeding prescription of IllustrisTNG where seeds of mass $8 \times 10^5\,\mathrm{M}_\odot$ are inserted in haloes which exceed a

threshold mass of $5 \times 10^{10}\,\mathrm{M}_\odot\,h^{-1}$ and do not already contain a BH (hereafter referred to as the 'TNG seed model').

Additionally, we explore the gas-based seeding prescriptions developed in and Bhowmick et al. (2021a, b). These are comprised of a combination of seeding criteria based on various gas properties of haloes. These criteria are designed such that our overall family of seed models broadly encompasses popular theoretical channels such as Pop III, NSC, and DCBH seeds, all of which exclusively form in regions comprised of dense, metal-poor gas. Here, we briefly summarize them as follows:

(i) *Dense, metal-poor gas mass criterion:* Seeds can only form in haloes that exceed a threshold for dense (>0.1 cm^{-3}), metal-poor ($Z < 10^{-4}\,Z_\odot$) gas mass, specified by $\tilde{M}_{\rm sf,mp}$ in the units of the seed mass $M_{\rm seed}$. $\tilde{M}_{\rm sf,mp}$ measures the amount of dense, metal-poor gas that is required to form a seed. There are no current constraints on $\tilde{M}_{\rm sf,mp}$, and we expect it to depend on the seeding channel. In this work, we explore models with $\tilde{M}_{\rm sf,mp} = 5$–$1000$.

(ii) *Halo mass criterion:* Seeds can only form in haloes that have exceeded a threshold for the total halo mass, specified by $\tilde{M}_h$ in the units of the seed mass $M_{\rm seed}$. In this work, we assumed a value of $\tilde{M}_h = 3000$, which ensures that our seeds of masses $\sim 10^4$–$10^6\,\mathrm{M}_\odot\,h^{-1}$ are only forming in haloes that have crossed the atomic cooling threshold (haloes with masses $\gtrsim 10^7\,\mathrm{M}_\odot$). The reason for this is twofold: (1) our simulations do not accurately model star formation in haloes below the atomic cooling threshold due to lack of H_2 cooling, and (2) massive ($\gtrsim 10^4\,\mathrm{M}_\odot$) DCBH seeds are expected to form only after the haloes cross the atomic cooling threshold.

(iii) *LW flux criterion:* In selected models, we also require the dense, metal-poor gas to be exposed to Lyman Werner (LW) fluxes above a critical value $J_{\rm crit}$. More specifically, seeds only form in haloes with a minimum threshold for dense, metal-poor, LW-illuminated gas mass, denoted by $\tilde{M}_{\rm sf,mp,LW}$ in the units of the seed mass $M_{\rm seed}$. Star formation is suppressed in these seed-forming regions. Given that our simulations do not contain full radiative transfer, the LW flux is computed using an analytic prescription described in Bhowmick et al. (2021a).

Our seed model is therefore described by four parameters, namely $\tilde{M}_{\rm sf,mp}$, $\tilde{M}_{\rm h}$, $J_{\rm crit}$, and $M_{\rm seed}$. All of our simulations include the first two parameters, and throughout the text the *dense, metal-poor gas mass criterion* and *halo mass criterion* are labelled as `SM*_FOF*` where the '*'s correspond to the values of $\tilde{M}_{\rm sf,mp}$ and $\tilde{M}_{\rm h}$. For example, $\tilde{M}_{\rm sf,mp} = 5$ and $\tilde{M}_{\rm h} = 3000$ will correspond to `SM5_FOF3000`. Runs which additionally apply the *LW flux criterion* contain an extra suffix `LW*` where '*' corresponds to $J_{\rm crit}$; for example, if a criterion with $J_{\rm crit} = 300\,J_{21}$ is added to `SM5_FOF3000`, it will be labelled as `SM5_FOF3000_LW300`. Lastly, the seed mass $M_{\rm seed}$ will be explicitly stated in the text and figure legends.

2.2 BH accretion and feedback models

BHs grow via a modified Bondi–Hoyle accretion prescription, with the maximum accretion rate limited to some factor $f_{\rm Edd} \geq 1$ times the Eddington accretion rate (which we refer to as the 'Eddington factor'):

$$\dot{M}_{\rm BH} = \min(\alpha \dot{M}_{\rm Bondi},\ f_{\rm edd}\dot{M}_{\rm Edd}) \tag{1}$$

$$\dot{M}_{\rm Bondi} = \frac{4\pi G^2 M_{\rm BH}^2 \rho}{c_{\rm s}^3} \tag{2}$$

$$\dot{M}_{\rm Edd} = \frac{4\pi G M_{\rm BH} m_p}{\epsilon_r \sigma_T\ c} \tag{3}$$

α is referred to as the 'Bondi boost' factor which is often used to boost the accretion rate to account for the inability to resolve the small-scale vicinity of the BH. G is the gravitational constant, ρ is the local gas density, $M_{\rm BH}$ is the BH mass, $c_{\rm s}$ is the local sound speed, m_p is the proton mass, and σ_T is the Thompson scattering cross-section. In practice, 'local' quantities are calculated as the kernel-weighted averages over nearby particles, typically those within a few $\times\ h^{-1}$pc. Accreting BHs radiate at luminosities given by

$$L = \epsilon_r \dot{M}_{\rm BH} c^2, \tag{4}$$

where ϵ_r is the radiative efficiency.

In the IllustrisTNG implementation, AGN feedback occurs both in 'thermal mode' as well as 'kinetic mode'. For Eddington ratios ($\eta \equiv \dot{M}_{\rm bh}/\dot{M}_{\rm edd}$) higher than a critical value of $\eta_{\rm crit} = \min[0.002(M_{\rm BH}/10^8 M_\odot)^2,\ 0.1]$, thermal energy is deposited on to the neighbouring gas at a rate of $\epsilon_{f,\rm high}\epsilon_r \dot{M}_{\rm BH} c^2$, where $\epsilon_{f,\rm high}\epsilon_r = 0.02$. $\epsilon_{f,\rm high}$ is called the 'high accretion state' coupling efficiency. If the Eddington ratio is lower than the critical value, kinetic energy is injected into the gas at irregular time intervals, which manifests as a 'wind' oriented along a randomly chosen direction. The injected rate is $\epsilon_{f,\rm low}\dot{M}_{\rm BH}c^2$ where $\epsilon_{f,\rm low}$ is called the 'low accretion state' coupling efficiency ($\epsilon_{f,\rm low} \lesssim 0.2$). For further details, we direct the interested readers to Weinberger et al. (2017).

The main parameters of our accretion model include the Bondi boost α, the radiative efficiency ϵ_r, and the Eddington factor $f_{\rm edd}$. The default values adopted in the `IllustrisTNG` suite are $\alpha = 1$, $\epsilon_r = 0.2$, and $f_{\rm edd} = 1$. We largely use this accretion model, and hereafter refer to it as the 'TNG accretion model'. However, we also run some simulations with different variations of these parameters, particularly when comparing our results to other studies. These variations include different combinations of $\alpha = 1$ and 100, $\epsilon_r = 0.2$ and 0.1, and $f_{\rm edd} = 1$–100. In the figure legends, these are labelled as `Boost*_RadEff*_EddFac*`, where the '*'s correspond to values of α, ϵ_r, and $f_{\rm edd}$, respectively.

2.3 Initial conditions: constrained Gaussian realizations

We expect the brightest $z > 6$ quasars to live in the rarest and most extreme overdensities in the Universe. In order to create initial conditions (ICs) that can produce such regions within a relatively small 9 cMpc$\,h^{-1}$ box, we apply the technique of *constrained Gaussian realizations* (CR). The CR method can efficiently sample a Gaussian Random field conditioned on various (user-specified) large-scale features. This technique was originally introduced by Hoffman & Ribak (1991) and van de Weygaert & Bertschinger (1996). We use the most recent implementation of this technique, i.e. the `GAUSSIANCR` code to generate the initial conditions. This code was fully developed by N21, wherein it was extensively tested against large-volume uniform cosmological simulations in terms of reproducing the halo assembly, star formation, and BH growth histories. Here, we briefly summarize the main features for completeness, while the full details of the underlying formalism are described in N21.

Overall, `GAUSSIANCR` constrains 18 parameters at the peak location (see N21 for details). In this work, we vary three parameters that were shown by N21 to be most consequential to BH growth. These are the following:

(i) The peak height 'ν' quantifies the 'rarity' of the peak by specifying its height in the units of the variance of $\delta_G(\mathbf{r})$ denoted by σ_{R_G}, i.e.

$$\nu \equiv \delta(\mathbf{r}_{\rm peak})/\sigma_{R_G}, \tag{5}$$

Table 1. The adopted values for the peak parameters for `5SIGMA`, `5SIGMA_COMPACT`, and `6SIGMA`. These constrained initial conditions (ICs) are characterized by the smoothing scale R_G (second column), the peak height ν (third column), the peak compactness x_d (fourth column), and the tidal scalar ϵ (fifth column); these four parameters are most consequential to BH growth. The remaining parameters do not significantly impact BH growth, and have been fixed to be the typical values of their underlying distributions (see fig. 5 of N21).

IC	R_G (Mpc h^{-1})	ν (σ_{R_G})	x_d (σ_2)	ϵ (km s^{-1} Mpc^{-1})
`5SIGMA`	1.0	5	3.6 (ave)	34.0 (ave)
`5SIGMA_COMPACT`	1.0	5	5.8 ($+3\sigma$)	15.0 (-2σ)
`6SIGMA`	1.3	6	4.0 (ave)	34.0 (ave)

$$\sigma^2_{R_G} \equiv \langle \delta_G(\mathbf{r})\delta_G(\mathbf{r})\rangle = \int \frac{P(k)}{(2\pi)^3}\hat{W}^2(k, R_G)\mathrm{d}k, \tag{6}$$

where $\mathbf{r}_{\rm peak}$ is the peak position, $P(k)$ is the power spectrum, and $\tilde{\delta}_G(\mathbf{r}) \equiv \int \tilde{\delta}(\mathbf{r})W(\mathbf{r}, R_G)$ is the overdensity smoothened over a scale R_G using the Gaussian window function $W(\mathbf{r}, R_G) = \exp(-r^2/2R_G^2)$ and its Fourier transform $\hat{W}(k, R_G) = \exp(-k^2R_G^2/2)$.

(ii) The peak compactness 'x_d' is set by the second-order derivatives of the smoothed overdensity field. More quantitatively, it is determined by the eigenvalues of the Hessian matrix $\partial_{ij}\delta_G$ ($i, j = 1, 2,$ and 3 are x, y, and z components, respectively) and can be parametrized as

$$\lambda_1 = \frac{x_d\sigma_2(R_g)}{1 + a_{12}^2 + a_{13}^2} \tag{7}$$

$$\lambda_2 = a_{12}^2\lambda_1 \tag{8}$$

$$\lambda_3 = a_{13}^2\lambda_1 \tag{9}$$

where $\sigma_2(R_g) \equiv \int \frac{P(k)}{(2\pi)^3}\hat{W}^2(k, R_G)k^2\mathrm{d}k$, and a_{12} and a_{13} are the axis ratios that determine the shape of the mass distribution around the ellipsoidal peak.

(iii) Lastly, the tidal strength ϵ is determined by second-order derivative of the gravitational potential i.e. the tidal tensor T_{ij} ($i = 1$, 2, 3). The eigenvalues of the tidal tensor can be parametrized by

$$\left[\epsilon\cos\frac{\omega + 2\pi}{3}, \epsilon\cos\frac{\omega - 2\pi}{3}, \epsilon\cos\frac{\omega}{3}\right], \tag{10}$$

where ϵ determines the overall magnitude of the tidal tensor, and ω determines the relative strengths of the tidal tensor along the three eigenvectors.

2.3.1 *Our choice of peak parameters*

N21 shows that BH growth is the most efficient within rare peaks (high ν) that are compact (high x_d) and allow for gas infall to occur from all directions (low tidal strength ϵ). Therefore, throughout this paper, we make intentional choices for ν, x_d, and ϵ and fix the remaining parameters at their most probable values (see fig. 5 of N21). Table 1 summarizes the adopted parameter values for ν, x_d, and ϵ. More specifically, we look at the following three regions:

(i) We choose a 5σ peak ($\nu = 5$) at scales of $R_G = 1$ Mpc h^{-1}, with x_d and ϵ corresponding to the typical values i.e. the maxima of their respective distributions. The peak height was chosen to produce a target halo mass of 10^{12} M$_\odot$ h^{-1} at $z = 7$. It is hereafter referred to as `5SIGMA`.

(ii) We again choose a 5σ peak at $R_G = 1$ Mpc h^{-1}, but with a compactness x_d that is 3σ away from the typical value, and a tidal strength ϵ that is -2σ away from the mean value. This also targets the assembly of a 10^{12} M$_\odot$ h^{-1} halo at $z = 7$, and is referred to as `5SIGMA_COMPACT`.

(iii) Lastly, we choose a 6σ peak ($\nu = 6$) at scales of $R_G = 1.3$ Mpc h^{-1} with typical values for x_d and ϵ. This targets a 5×10^{12} M$_\odot$ h^{-1} halo at $z = 7$, and is referred to as `6SIGMA`.

Note that the target haloes produced in `6SIGMA` and `5SIGMA_COMPACT` regions have number densities roughly similar to those of the observed $z \sim 6$ quasars ($\sim$1 Gpc^{-3}). In contrast, `5SIGMA` produces a target halo that is $\sim$100 times more common.

Finally, we also note that the BH growth can depend on the specific realization of the large-scale density field. However, upon exploring five different realizations for a select few BH models, we found that the differences in BH growth were mild ($z \sim 6$ BH masses vary by factors $\lesssim$2).

2.4 Simulation resolution

In Bhowmick et al. (2021a, b), we performed detailed resolution convergence tests for our BH seed model and found that for our fiducial model with $\tilde{M}_{\rm sf,mp} = 5$ and $\tilde{M}_h = 3000$, the seed formation rates are reasonably well converged for gas mass resolutions $\lesssim 10^4$ M$_\odot$ h^{-1}. The resolution convergence becomes slower as the models are made more restrictive by increasing $\tilde{M}_{\rm sf,mp}$ or by introducing an LW flux criterion. As we shall see in Section 3.5, the resolution convergence properties of our constrained regions are similar to that of the zoom region of Bhowmick et al. (2021a, b).

To achieve a gas mass resolution of $\sim 10^4$ M$_\odot$ h^{-1} in a box size of 9 Mpc h^{-1}, we need $N = 720$ DM particles per dimension (note that the number of gas cells are initially assigned to be equal to the DM particles, but as the simulations evolve the gas cells can undergo refinement or de-refinement). However, running such a simulation until $z = 6$ requires a substantial amount of computing time and memory, particularly in regions with extreme overdensities. Therefore, to facilitate a rapid exploration of the large parameter space of our seed models, we choose $N = 360$ (DM particle mass $= 1.1 \times 10^6$ M$_\odot$ h^{-1}). We assign this to be our fiducial resolution, and it corresponds to a gas mass resolution of $\sim 10^5$ M$_\odot$ h^{-1}. Note that this is only slightly lower than the highest resolution box of the `IllustrisTNG` suite i.e. TNG50. That being said, we do run higher resolution realizations ($N = 720$, DM particle mass $= 1.4 \times 10^5$ M$_\odot$ h^{-1}) for a few selected models, particularly those that successfully produce a $z \gtrsim 6$ quasar. As we shall see in Section 3.5, the final BH mass at $z \lesssim 7$ is not significantly impacted by resolution. Additionally, we use the $N = 720$ runs to probe the lowest seed mass considered in this work i.e. $M_{\rm seed} = 1.25 \times 10^4$ M$_\odot$ h^{-1}. The fiducial $N = 360$ run can only probe seed masses of $M_{\rm seed} = 1 \times 10^5$ and 8×10^5 M$_\odot$ h^{-1}. Hereafter, unless otherwise stated, we are using $N = 360$. For runs that use $N = 720$, it shall be explicitly stated in the captions or the text.

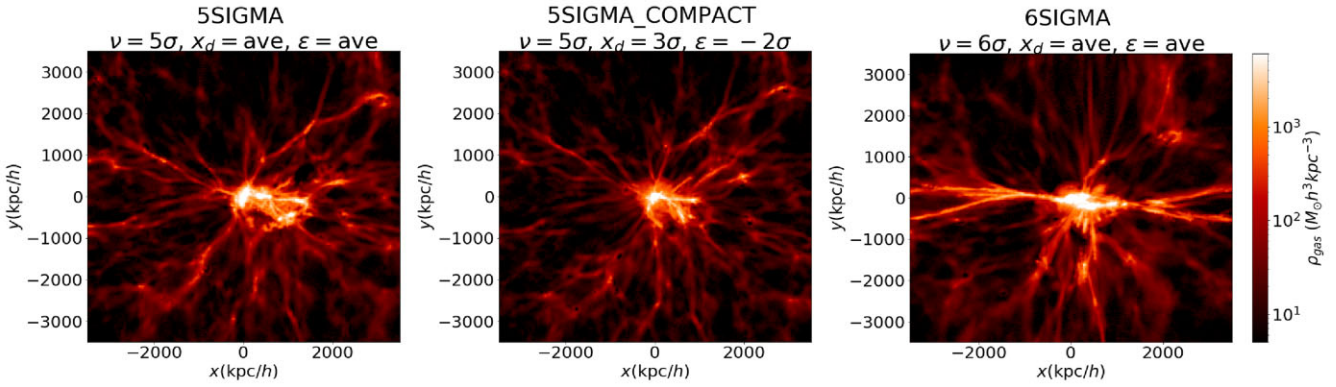

Figure 1. Projected gas density field at the $z = 6$ snapshot for the three constrained Gaussian initial conditions we explored in this work. The thickness of the slices is 50 kpc h^{-1}. The left-hand panel is centred at a 5σ overdensity peak at $R_G = 1$ Mpc h^{-1}, and typical values for compactness x_d and tidal strength ϵ; this is hereafter referred to as 5SIGMA. The middle panel is centred at a 5σ overdensity peak with $+3\sigma$ higher compactness, and -2σ lower tidal strength; we refer to this as 5SIGMA_COMPACT. The right-hand panel is centred at a 6σ overdensity peak at $R_G = 1.3$ Mpc h^{-1} with average values of compactness and tidal strength; this is referred to as 6SIGMA. We can see that the gas distribution in 5SIGMA_COMPACT is more isotropic and centrally concentrated compared to 5SIGMA and 6SIGMA.

3 RESULTS

3.1 Halo environments: evolution from $z \sim 20$–6

Before looking at the properties of BHs, we first look at the environments in which they form and grow. Fig. 1 shows the $z = 6$ gas density profiles centred at the location of the constrained 5SIGMA, 5SIGMA_COMPACT, and 6SIGMA peaks. Visually, we can clearly see that the gas distribution around the 5SIGMA_COMPACT peak is more compact and isotropic compared to that of 5SIGMA and 6SIGMA. Fig. 2 shows the evolution of the most massive halo (MMH) from $z \sim 20$ to 6, in terms of the total mass, gas mass, and stellar mass. We see that both 5SIGMA_COMPACT, and 5SIGMA runs assemble their target mass of $\sim 10^{12}\,\mathrm{M}_\odot\,h^{-1}$ by $z = 7$, which grows to become $\sim 2 \times 10^{12}\,\mathrm{M}_\odot\,h^{-1}$ by $z = 6$. The 6SIGMA run assembles halo masses of $\sim 7 \times 10^{12}\,\mathrm{M}_\odot\,h^{-1}$ and $\sim 10^{13}\,\mathrm{M}_\odot\,h^{-1}$ by $z = 6$.

Interestingly, the halo assembly history (see Fig. 2: top panel) of the three regions shows that for 5SIGMA_COMPACT, the MMHs at $z \gtrsim 10$ are ∼5–10 times more massive compared to that of 5SIGMA (as well as 6SIGMA). But at $z \lesssim 10$, the halo growth rate for the 5SIGMA_COMPACT run becomes slower compared to the 5SIGMA run, thereby explaining the similar final halo masses that both the runs assemble at $z \sim 6$–7. That is likely because the MMH in the 5SIGMA_COMPACT peak becomes more isolated at $z \lesssim 10$ (after having merged with most of its neighbouring massive haloes by $z \sim 10$). However, the 5SIGMA_COMPACT MMH continues to become more dense during $z \sim 9$–6 (due to continued gravitational collapse), which likely causes the higher compactness of 5SIGMA_COMPACT peak compared to 5SIGMA (as well as 6SIGMA) at $z \sim 6$–7.

The evolution of the gas mass (see Fig. 2: middle panel) mirrors that of the total halo mass at $z \sim 20$–10. More specifically, the gas mass of the MMH in 5SIGMA_COMPACT is ∼5–10 times higher than that of 5SIGMA and 6SIGMA (similar to the total halo mass) at $z \sim 20$–10. Notably, we find that at $z \sim 9$–6, there is no significant increase in the gas mass for the MMH in 5SIGMA_COMPACT, unlike the MMHs of 5SIGMA and 6SIGMA. As a result, by $z = 6$, the MMH in 5SIGMA_COMPACT ends up with a lower gas mass compared to 5SIGMA and 6SIGMA. As we shall see, this is happening because the gas in 5SIGMA_COMPACT is being rapidly consumed by star formation and BH accretion, more so than 5SIGMA and 6SIGMA. The enhanced star formation in 5SIGMA_COMPACT can be seen in the bottom panel of Fig. 2, wherein the stellar mass is ∼7 times higher than that of 5SIGMA at $z \sim 6$–7 (making it similar to the stellar mass produced by 6SIGMA at $z \sim 6$–7). The 5SIGMA_COMPACT region therefore produces an overly massive galaxy for its host halo mass, as clearly seen in Fig. 3. Fig. 3 also demonstrates that our constrained runs are consistent with the stellar mass versus halo mass relations predicted by TNG300, thereby validating this technique.

Having discussed the evolution of the global properties of the MMH, we now focus on the evolution of their internal gas distributions, which are much more consequential to BH growth. The evolution of the radially averaged gas density profiles from $z \sim 14$ to 6 is shown in Fig. 4. In all three regions, little evolution occurs at $z \gtrsim 9$, and the central ∼1 kpc h^{-1} is unresolved owing to low gas densities. In the range $z \sim 9$–6 however, the gas densities start to significantly increase, particularly close to the halo centres. Specifically, while the overall gas mass of the MMH only increases by factors of ∼50 between $z \sim 9$ and 6 (Fig. 2: middle panel), the central gas densities increase by factors of ∼100–10 000 during the same time interval. Amongst the three regions, 5SIGMA_COMPACT shows the steepest increase in density between $z \sim 9$ and 6. Fig. 5 shows the 2D colour maps of the evolution of the gas density, star formation rates, and metallicity for 5SIGMA_COMPACT region at redshift snapshots of $z = 12, 10, 8,$ and 6. We can clearly see that the steep increase in central gas density leads to a commensurate boost in the star formation, as well as metal enrichment in the central regions of the halo. As we shall see, this increase in the central gas densities leads to substantially increased importance of accretion-driven BH growth at $z \sim 9$–6.

3.2 BH growth in different halo environments: impact of BH seeding models

We are particularly interested in the growth histories of BHs occupying the MMH in each region. Fig. 6 shows the number of BHs that are present within the MMH at different redshift snapshots, with different panels showing different seed models. We note that these MMHs tend to acquire several BHs during their assembly history. Despite many of these BHs inevitably merging with the central BH, the overall number of BHs hosted by the MMHs increases up to at least $z \sim 9$–10. This is because the MMHs continue to acquire

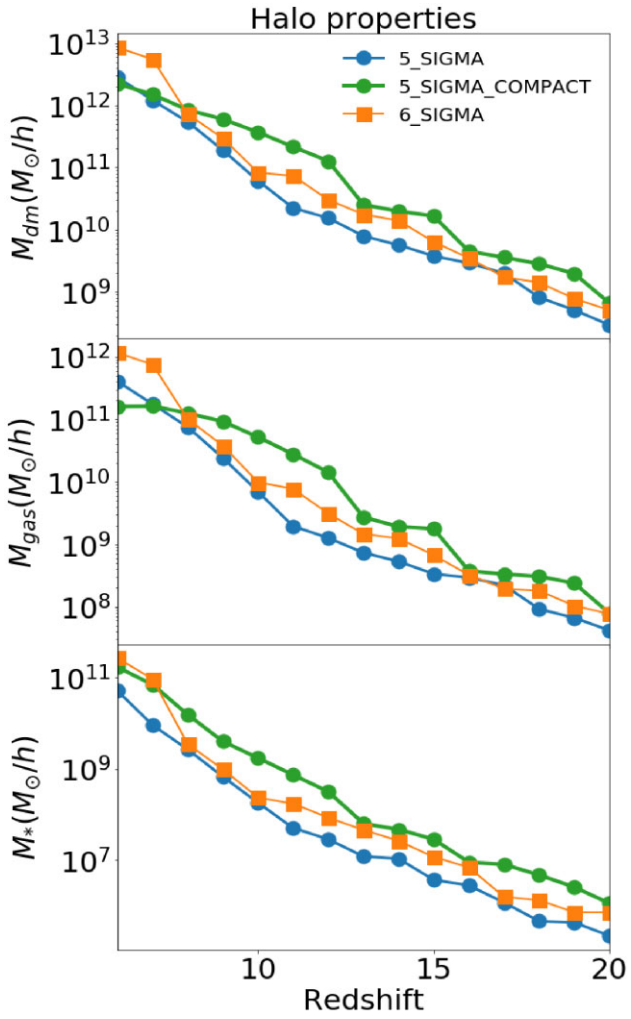

Figure 2. The evolution of the most massive halo (MMH) from $z \sim 20$ to $z \sim 6$ for 5SIGMA (blue), 5SIGMA_COMPACT (green), and 6SIGMA (orange) lines. The top, middle, and bottom panels show the total halo mass, gas mass, and stellar mass, respectively. For 5SIGMA and 5SIGMA_COMPACT, we reach our target halo mass of $\sim 10^{12}\,\mathrm{M}_\odot\,h^{-1}$ at $z = 7$; they both assemble a total gas mass of $2 \times 10^{11}\,\mathrm{M}_\odot\,h^{-1}$. Likewise, the 6SIGMA volume assembles the desired target halo mass of $6 \times 10^{12}\,\mathrm{M}_\odot\,h^{-1}$ at $z = 7$, and a gas mass of $5 \times 10^{11}\,\mathrm{M}_\odot\,h^{-1}$. 5SIGMA_COMPACT assembles a stellar mass of $\sim 10^{11}\,\mathrm{M}_\odot\,h^{-1}$ at $z = 7$, similar to that of 6SIGMA; this is significantly higher than 5SIGMA which assembles a stellar mass of $9 \times 10^9\,\mathrm{M}_\odot\,h^{-1}$. More compact peaks (at fixed peak height) lead to enhanced star formation.

new BHs from surrounding merging haloes. At $z = 6$, the MMHs can generally host up to ∼10–50 BHs depending on the constrained region as well as the seed model.

Next, we look at how the number of BHs in the MMHs vary between different regions and seed models. For all seed models, we generally see that the 5SIGMA_COMPACT runs tend to start forming seeds at earlier times, and therefore host a higher number of BHs at $z \sim 10$–20 compared to 5SIGMA and 6SIGMA runs. This is because the MMHs at $z \sim 10$–20 for the 5SIGMA_COMPACT runs are more massive compared to the other two regions (revisit Fig. 2). However, between $z \sim 10$ and 6, we find that there is no significant increase in the number of BHs for the MMH in 5SIGMA_COMPACT, unlike 5SIGMA and 6SIGMA. This is likely because in the 5SIGMA_COMPACT runs, most of the nearby massive haloes have already merged with the MMH by $z \sim 10$, leaving behind

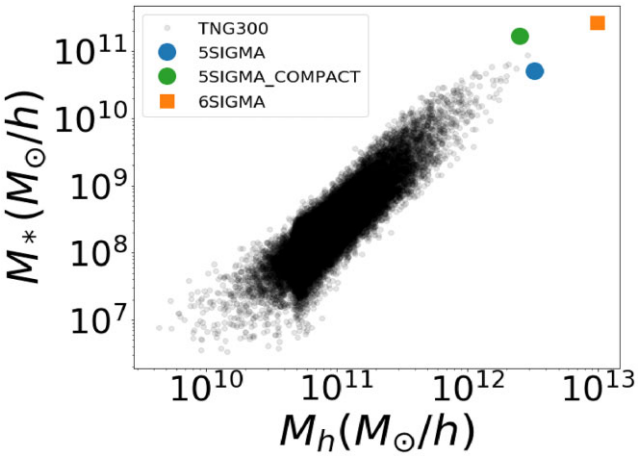

Figure 3. Stellar mass versus halo mass relation at $z = 6$ for the MMHs of 5SIGMA_COMPACT (green), 5SIGMA (blue), and 6SIGMA (orange), respectively, compared with the full halo population of TNG300 (a [300 Mpc]^3 box – the largest volume in the IllustrisTNG simulation suite; faded grey circles). The predictions from the constrained runs are broadly consistent with the trends extrapolated from the TNG300 results. The 5SIGMA and 6SIGMA runs produce stellar mass predictions close to the mean trend, whereas the 5SIGMA_COMPACT run produces a somewhat overly massive galaxy (stellar mass) compared to its host halo.

an isolated MMH during $z \sim 10$–6 with very few nearby haloes to acquire new BHs from. On the other hand, for the 5SIGMA and 6SIGMA runs, the MMHs are not as isolated at $z \sim 10$–6, and they continue to acquire new BHs during this time. All of this ultimately leads to fewer BHs in the MMH of 5SIGMA_COMPACT at $z = 6$, compared to 5SIGMA and 6SIGMA regions. Lastly, note that the TNG seed model (Fig. 6: left-hand panel) is substantially more restrictive and produces much fewer seeds compared to our fiducial gas-based seed models with $\tilde{M}_{\rm sf,mp} = 5$, $\tilde{M}_{\rm h} = 3000$ (hereafter SM5_FOF3000 shown in Fig. 6: middle and right-hand panels).

The primary science focus of this work is the growth of the most massive BH located in the MMH of our simulations. So unless otherwise stated, all future references to BH growth histories are for the most massive BH at $z = 6$ in each simulation. Fig. 7 shows the BH growth histories for 5SIGMA, 5SIGMA_COMPACT, and 6SIGMA. We first focus on the halo-based TNG seed model (leftmost panels), which starts to seed BHs around $z \sim 10$–12. Note that for this seed model, very few BHs are formed overall, which results in very little growth via mergers (see dashed lines in Fig. 7: top left panel). We find that amongst all three regions, 5SIGMA_COMPACT assembles the highest mass BH at $z = 6$, despite containing the least number of BHs within its MMH (also recall that 6SIGMA has a higher mass MMH at $z = 6$). This is because the 5SIGMA_COMPACT run produces a higher gas density at the peak location, thereby leading to the fastest growth via gas accretion at $z \lesssim 9$. This result is overall consistent with N21, showing that compact peaks with low tidal fields are the most ideal environments for rapid BH growth. However, with this TNG seed model, the overall BH mass assembled at $z = 6$ is only $\sim 5 \times 10^7\,\mathrm{M}_\odot$, which is significantly smaller than the typical masses of the observed high-z quasars ($\sim 10^9\,\mathrm{M}_\odot$).

Next, we look at the predictions from gas-based seed models, particularly SM5_FOF3000 ($\tilde{M}_{\rm sf,mp} = 5$ and $\tilde{M}_{\rm h} = 3000$) with seed masses of 8×10^5 and $1 \times 10^5\,\mathrm{M}_\odot\,h^{-1}$ (Fig. 7: middle and right-hand panels, respectively). Again, these models produce substantially higher numbers of seeds that start forming at much earlier times ($z \sim 17$–25) compared to the TNG seed model. As a result, there is

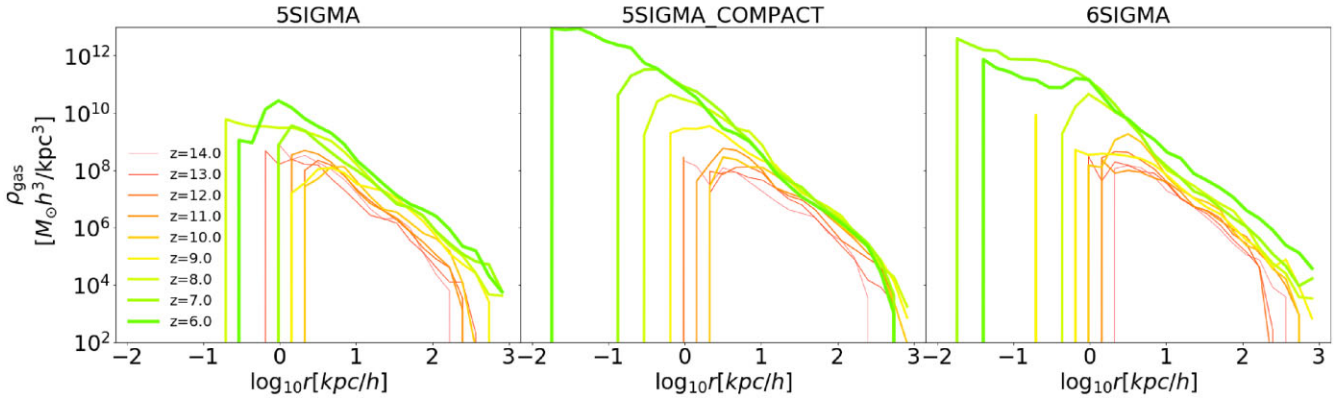

Figure 4. Radially averaged 1D profiles of the gas density (physical units), centred around the most massive BH in the MMH of our simulation volume for 5SIGMA, 5SIGMA_COMPACT, and 6SIGMA. The lines of different colours show the redshift evolution from $z = 14$ to $z = 6$. We see that gas density in the central regions steeply increases with time between $z \sim 9$ and 6. The steepest increase is seen for 5SIGMA_COMPACT.

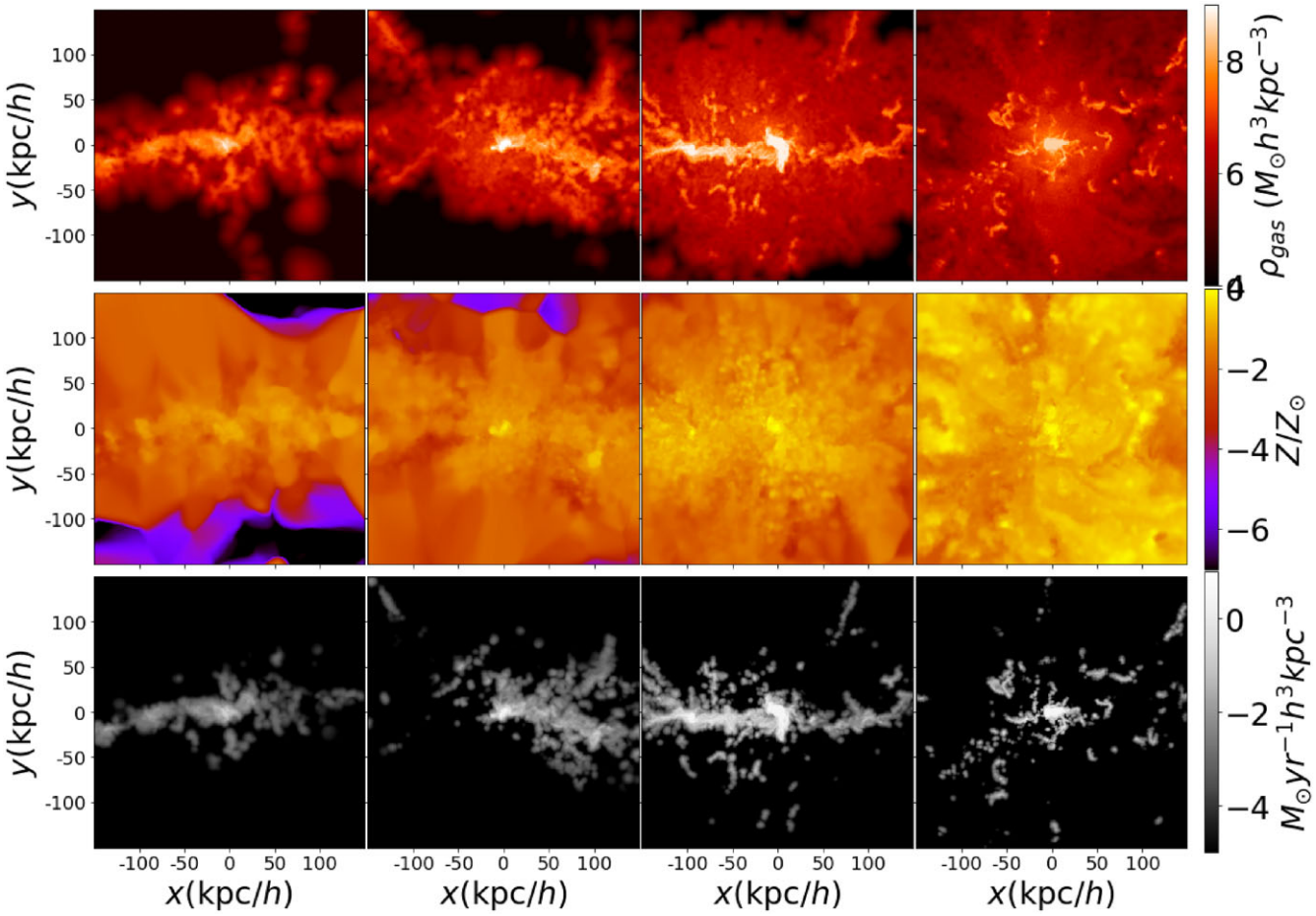

Figure 5. 2D profiles of the gas density, metallicity, and the star formation rate density (densities are in physical units) within the vicinity of the most massive BH in the MMH of the 5SIGMA_COMPACT run. We compute these quantities averaged over a slice of thickness 10 kpc h^{-1}. The left- to right-hand panels show the redshift evolution from $z = 10$ to $z = 6$. At $z \lesssim 9$, the steep increase in the gas density leads to increase in the star formation and metal enrichment in the halo.

now considerable growth via mergers. To that end, we note that regardless of how early the seeds form, accretion-driven BH growth does not become significant until $z \lesssim 9$ (see the second rows of Fig. 7). This results from the fact that the central gas densities remain relatively low until $z \sim 9$ but start to steeply increase between $z \sim 9$ and 6 (revisit Fig. 4). As a result, the BH growth at $z \gtrsim 9$ is completely driven by BH mergers. In fact, for SM5_FOF3000 seed models, the $z \gtrsim 9$ merger-driven growth assembles a BH mass of $\sim 3 \times 10^7$ $M_\odot$ by $z \sim 9$, in contrast to the TNG seed model where the BHs are still close to the seed mass of $\sim 10^6$ $M_\odot$ at $z \sim 9$. Between

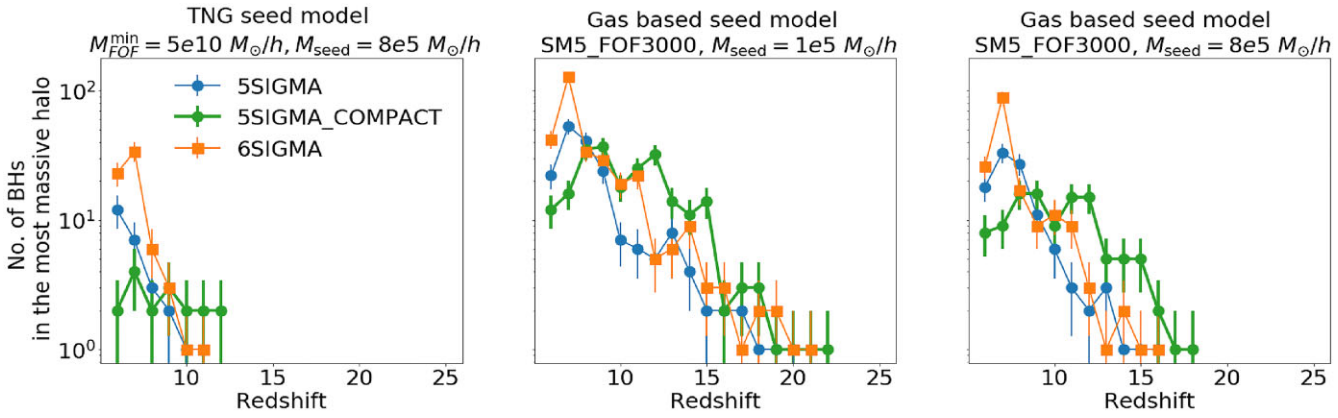

Figure 6. Number of BHs present in the MMH at different redshift snapshots for 5SIGMA (blue), 5SIGMA_COMPACT (green), and 6SIGMA (orange) lines. Error-bars correspond to Poisson errors. In the leftmost panel, we use the default seeding prescription from the IllustrisTNG simulation suite (referred to as TNG seed model). In the middle and right-hand panels, we use the gas-based seeding prescription with $\tilde{M}_h = 3000$ and $\tilde{M}_{\rm sf,mp} = 5$ (SM5_FOF3000). All these runs use the default accretion prescription from the IllustrisTNG simulation suite (TNG accretion model). We see that the onset of seed formation happens earliest within the 5SIGMA_COMPACT run; therefore, it contains the highest number of BHs around $z \gtrsim 10$. However, between $z \sim 9$ and 6, the 5SIGMA_COMPACT does not acquire many new BHs. On the other hand, the 5SIGMA and 6SIGMA MMHs continue to acquire new BHs from nearby haloes between $z \sim 9$ and 6. Therefore, by $z = 6$, the 5SIGMA_COMPACT peak has the least number of BHs and 6SIGMA peak has the highest number of BHs.

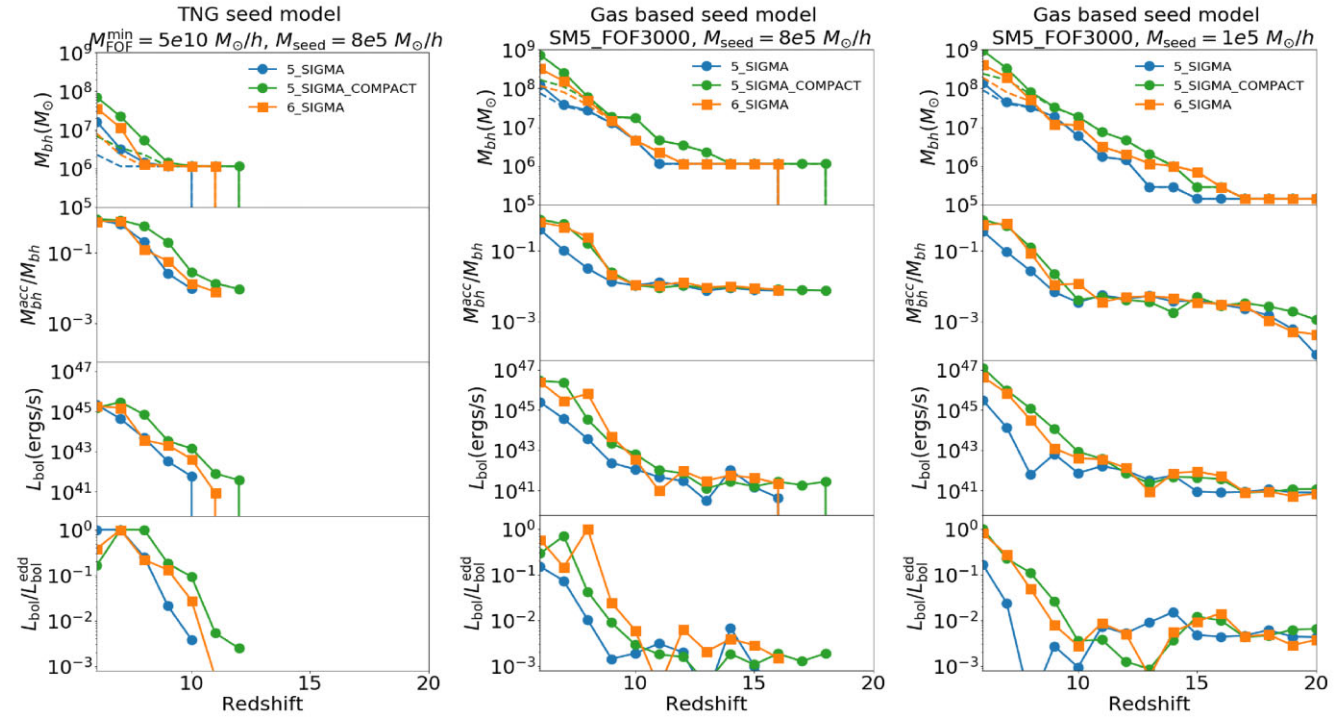

Figure 7. Evolution of the most massive BH at $z = 6$ in the MMH of 5SIGMA (blue), 5SIGMA_COMPACT (green), and 6SIGMA (orange) lines (hereafter, all growth histories plotted for different runs are for this particular BH in each simulation). The first row corresponds to the BH mass; the solid lines show the total BH mass and the dashed lines show the mass accumulated only by mergers. The second row shows the fraction of the current mass accumulated by gas accretion. The third and fourth rows show the total bolometric luminosity in units of erg s^{-1} and the Eddington luminosity, respectively. All the runs use the TNG accretion model. In the left-hand panels, we use the TNG seed model. In the middle and right-hand panels, we use the gas-based seeding prescription SM5_FOF3000. The BH seed mass is 8×10^5 and $1 \times 10^5 M_\odot\, h^{-1}$ in the middle and right-hand panels, respectively. Among the constrained volumes we explore, 5SIGMA_COMPACT assembles the highest BH mass in all cases. Even in this region, the TNG seed model achieves a maximum BH mass of $\sim 7 \times 10^7$ M$_\odot\, h^{-1}$ by $z = 6$, which is significantly smaller than the typical masses of observed $z \sim 6$ quasars. In contrast, the SM5_FOF3000 models are able to assemble 10^9 M$_\odot\, h^{-1}$ SMBHs by $z = 6$. While these massive BHs are active as luminous quasars with near-Eddington luminosities of $\sim 10^{47}$ erg s^{-1} at $z = 6$, their growth at $z \gtrsim 9$ is dominated by BH mergers. Overall, the BH growth is fastest within rare massive high-z haloes that are also sufficiently compact and have low tidal fields. To produce $z \sim 6$ quasars in these haloes with the TNG accretion model, an early boost in BH mass driven by mergers is necessary.

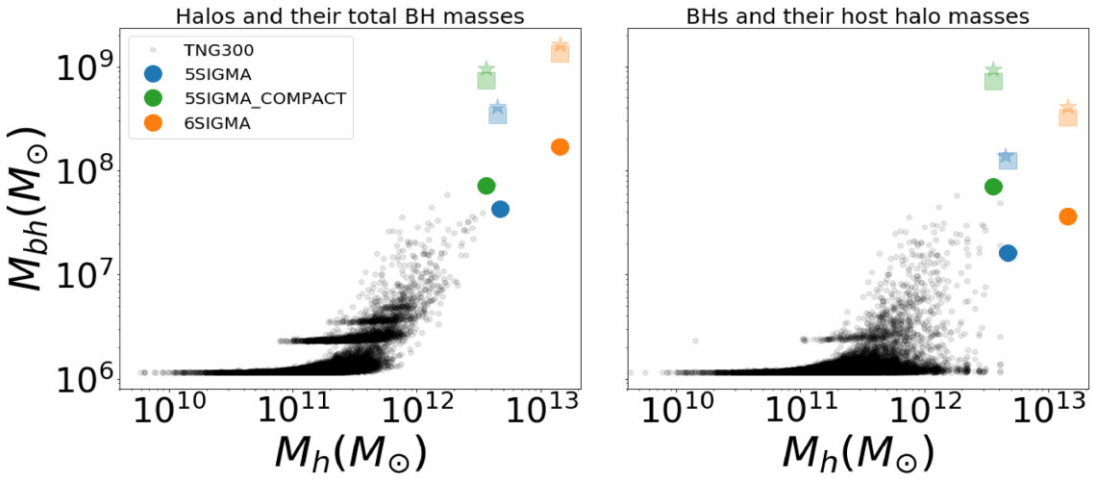

Figure 8. BH mass versus halo mass scaling relation at $z = 6$. In the left-hand panel, each data point corresponds to a halo, so we are plotting the 'halo mass versus total mass of all BHs in the halo', for all haloes at $z = 6$. In the right-hand panel, each data point corresponds to a BH, so we are plotting the 'BH mass versus host halo mass', for all individual BHs at $z = 6$. The blue, green, and orange colours correspond to the BH within the MMH of `5SIGMA`, `5SIGMA_COMPACT`, and `6SIGMA` regions, respectively. All the runs use the TNG accretion model. The circles correspond to the TNG seed model, which we directly compare to the full population of TNG300. The left-hand panels show that for the TNG seed model, the total BH masses of MMHs produced by the constrained runs are consistent with the extrapolated trends from the TNG300 population. This further validates our constrained runs. The squares and stars correspond to the gas-based seed model `SM5_FOF3000` with seed masses of 8×10^5 and $1 \times 10^5\,M_\odot\,h^{-1}$, respectively; these models produce much higher BH masses compared to the TNG seed model. The MMHs generally tend to host a significantly large number of BHs during their assembly history, generally ranging between ∼10 and 50 depending on the constrained region as well as the seed model (revisit Fig. 6). The `6SIGMA` run produces the highest number of BHs and also the highest total BH mass in its target halo, commensurate with its halo mass. However, when we look at masses of *individual* BHs in the right-hand panel, the most massive BH is actually produced by `5SIGMA_COMPACT`. In fact, with the `SM5_FOF3000` seed model, only the `5SIGMA_COMPACT` can produce *individual* $\sim 10^9\,M_\odot\,h^{-1}$ BHs similar to the observed $z \sim 6$ quasars.

$z \sim 9$ and 6, the accretion-driven BH growth becomes increasingly significant for the `SM5_FOF3000` seed models, pushing the BH mass to values $\gtrsim 10^8\,M_\odot$ at $z = 6$ for all three constrained regions. Amongst the three regions, `5SIGMA_COMPACT` again produces the highest BH mass that now reaches close to $\sim 10^9\,M_\odot$ at $z = 6$, consistent with the observed $z \sim 6$ quasars. Additionally, note that the merger-driven growth can also be boosted, by simply reducing the halo mass threshold and forming more seeds. Therefore, $z \sim 6$ quasars could also be formed within a 'halo mass only' seed model (e.g. TNG seed model) with a sufficiently low halo mass threshold.

The bolometric luminosities and Eddington ratios (see the third and fourth rows of Fig. 7) of the BHs remain low ($L_{\rm bol} \sim 10^{42}$ erg s^{-1} $\sim 10^{-3}$ $L^{\rm edd}_{\rm bol}$) at $z \gtrsim 9$ wherein the accretion-driven BH growth is insignificant. This is generally true for all seed models and constrained regions. As we go from $z \sim 9$ to 6 during which the central gas densities steeply rise (revisit Fig. 4), the accretion-driven BH growth becomes increasingly efficient. This leads to a sharp increase in the BH luminosities. By $z \sim 6$, the BHs start to grow close to the Eddington limit for all of the runs, generally corresponding to bolometric luminosities $\gtrsim 10^{45}$ erg s^{-1}. However, luminosities of observed $z \sim 6$ quasars are even higher i.e. $\sim 10^{47}$ erg s^{-1}. These luminosities are produced only by the $\sim 10^9\,M_\odot$ BHs that are formed within `5SIGMA_COMPACT` region using the `SM5_FOF3000` seed models. Overall, we find that to form BHs that resemble the observed $z \sim 6$ quasars (masses of $\sim 10^9\,M_\odot$ and luminosities of $\sim 10^{47}$ erg s^{-1}) in our simulations with `IllustrisTNG` physics, we need massive compact haloes with seed models such as `SM5_FOF3000` that allow for substantial merger-driven BH growth at $z \gtrsim 9$.

Fig. 8 shows the predictions of our constrained runs the $z = 6$ halo, as well as the BH populations in the TNG300 uniform simulation. Note that the most massive $z = 6$ BHs produced by TNG300 are ∼50 times smaller than the observed $z \gtrsim 6$ quasars. This is simply because TNG300 does not have the volume to produce such rare objects, despite being among the largest simulations to be run past $z = 6$ and beyond. In fact, this is true for almost all major cosmological hydrodynamic simulations run to date (see Habouzit et al. 2021, 2022a, b for combined analyses of BH populations from several simulations). The only exception to this would be the `BlueTides` simulation (Feng et al. 2016) which produces a $6.4 \times 10^8\,M_\odot$ BH in a volume of $[400\,{\rm Mpc}\,h^{-1}]^3$ by $z \sim 7.5$ (Tenneti et al. 2019). Overall, this further highlights the power of our constrained simulations which is able to produce such rare objects within smaller volume and higher resolution simulations in reasonable computing time, so as to allow an exploration of a wide range of model parameters.

We now specifically compare the BHs produced in the MMHs of the constrained runs to that of the TNG300 simulation. The left-hand panel of Fig. 8 shows the halo mass versus the total mass of all BHs within the haloes. We find that for the TNG seed model, predictions for the constrained runs are consistent with extrapolation of the BH mass versus halo mass relation from TNG300. These results, together with the stellar mass versus halo mass relations in Fig. 3, serve as a good validation for our constrained runs. As expected from the results in the previous paragraph, the gas-based seed models `SM5_FOF3000` produce haloes with total BH masses that are significantly higher than the extrapolated trend of the TNG300 haloes. As an additional note, the M_{bh}–M_h relation for the lowest mass BHs within TNG300 form streaks of horizontal lines that can be clearly seen in Fig. 8. This is likely an artefact of the TNG seed model, where BHs seeded within $\gtrsim 10^{10}\,M_\odot$ haloes do not show significant accretion-driven growth until haloes reach masses $\gtrsim 10^{11}\,M_\odot$.

Closer examination of Fig. 8 (left-hand panel) reveals another interesting result. For the TNG seed model as well as the gas-based

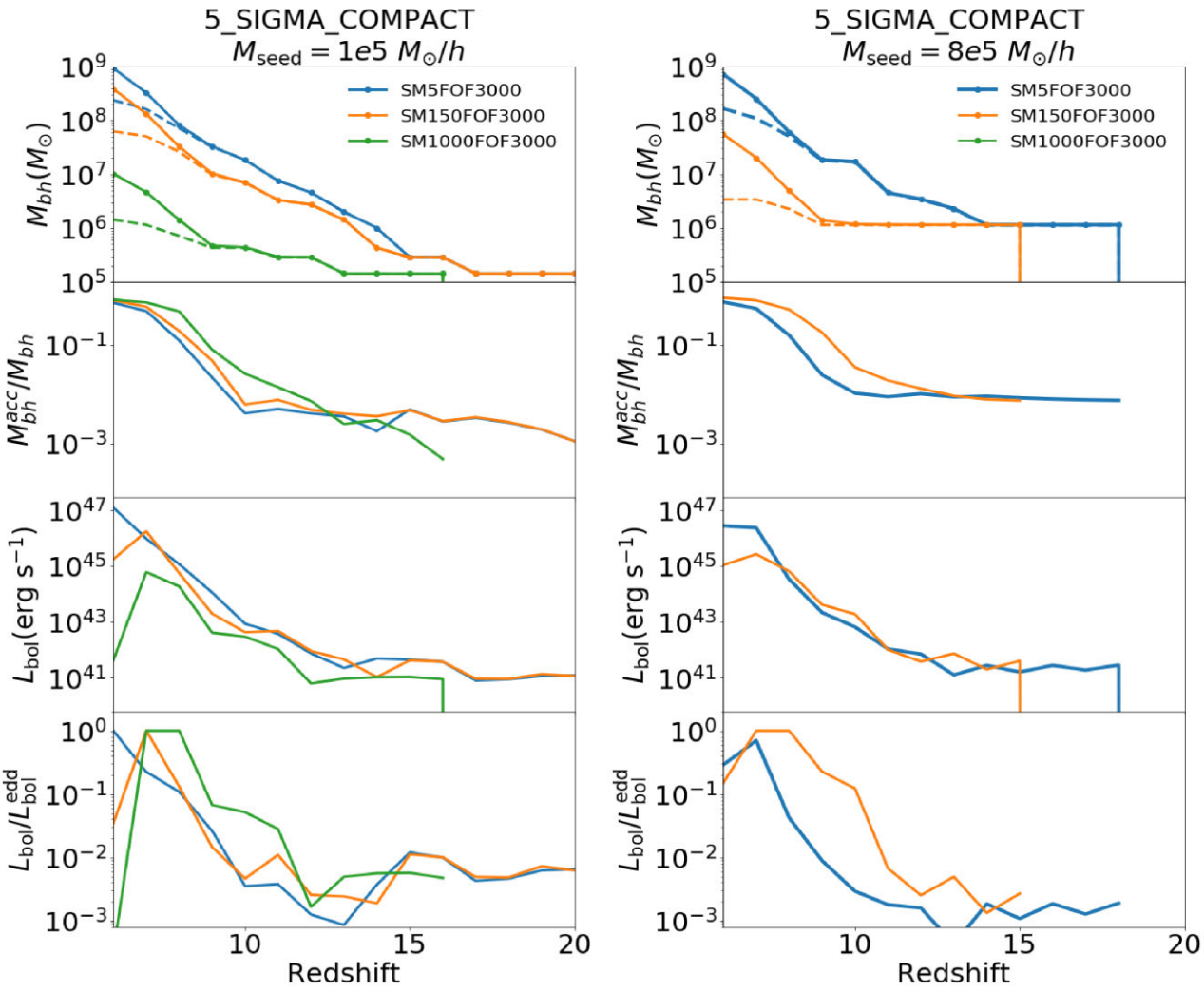

Figure 9. Evolution of the most massive BH in 5SIGMA_COMPACT for $\tilde{M}_{sf,mp} = 5$, 150, and 1000. The left- and right-hand panels correspond to seed masses of 10^5 and $8 \times 10^5\ M_\odot\ h^{-1}$, respectively. Note that the SM1000FOF3000 model does not produce a $8 \times 10^5\ M_\odot\ h^{-1}$ seed, which is why there are no green lines on the right-hand panel. All the runs here use the TNG accretion model. The different rows show the same set of quantities as Fig. 7. As the seeding criteria becomes more stringent, there are fewer mergers to grow the BH at $z \gtrsim 9$. As a result, the final $z = 6$ BH mass decreases and falls significantly short of producing the observed $z \sim 6$ quasars.

seed model, the MMH in 6SIGMA achieves the highest *total* BH mass. This contrasts with Fig. 7 and with the right-hand panel of Fig. 8, which clearly show that 5SIGMA_COMPACT produces the highest *individual* BH mass in the MMH. As it turns out, while the MMHs in 5SIGMA and 6SIGMA end up with a higher number of BHs than 5SIGMA_COMPACT (revisit Fig. 6), the individual BHs in 5SIGMA and 6SIGMA are significantly smaller than the most massive BH in 5SIGMA_COMPACT. The foregoing statement is generally true for TNG seed model as well as the gas-based seed models. Particularly for the gas-based seed model SM5_FOF3000, this means that while a typical rare massive halo ($\sim 10^{13}\ M_\odot$) at $z \sim 6$ can acquire total BH mass exceeding $\sim 10^9\ M_\odot$, it may not produce 'individual BHs' of such masses. Therefore, to host the observable $z \gtrsim 6$ quasars that correspond to individual $\sim 10^9\ M_\odot$ BHs growing close to the Eddington limit, we need haloes that are not just massive enough, but are also highly compact and have low tidal fields. In these compact MMHs, the BHs are more likely to have close encounters with each other. Therefore, they can merge more readily to form a single massive BH at the halo centres, compared to typical haloes of the same mass. To that end, recall that the small-scale dynamics are poorly resolved in our simulations, particularly for lower mass BHs. Several recent works with more realistic treatment of BH small-scale dynamics (for e.g. Tremmel et al. 2017, 2018; Chen et al. 2022; Ni et al. 2022) have found that many of the seeds (particularly lower mass seeds) do not sink efficiently to the local potential minima, thereby leading to a population of wandering BHs (Tremmel et al. 2018; Ma et al. 2021; Ricarte et al. 2021a, b; Weller et al. 2022). Therefore, prompt mergers resulting from our current BH repositioning scheme could overestimate the rate at which the central BH grows. In future work, we shall investigate this in the context of the assembly of the $z \sim 6$ quasars.

Next, we focus on the 5SIGMA_COMPACT region and further explore different variations of gas-based seeding models to study their impact on BH growth. Note that SM5_FOF3000 ($\tilde{M}_{sf,mp} = 5$ & $\tilde{M}_h = 3000$), which successfully produces a $z \sim 6$ quasar, is the least restrictive amongst the family of BH seeding models developed in Bhowmick et al. (2021a, b). Fig. 9 shows the impact of further increasing $\tilde{M}_{sf,mp}$ to values of 150 and 1000, on the BH mass, lumi-

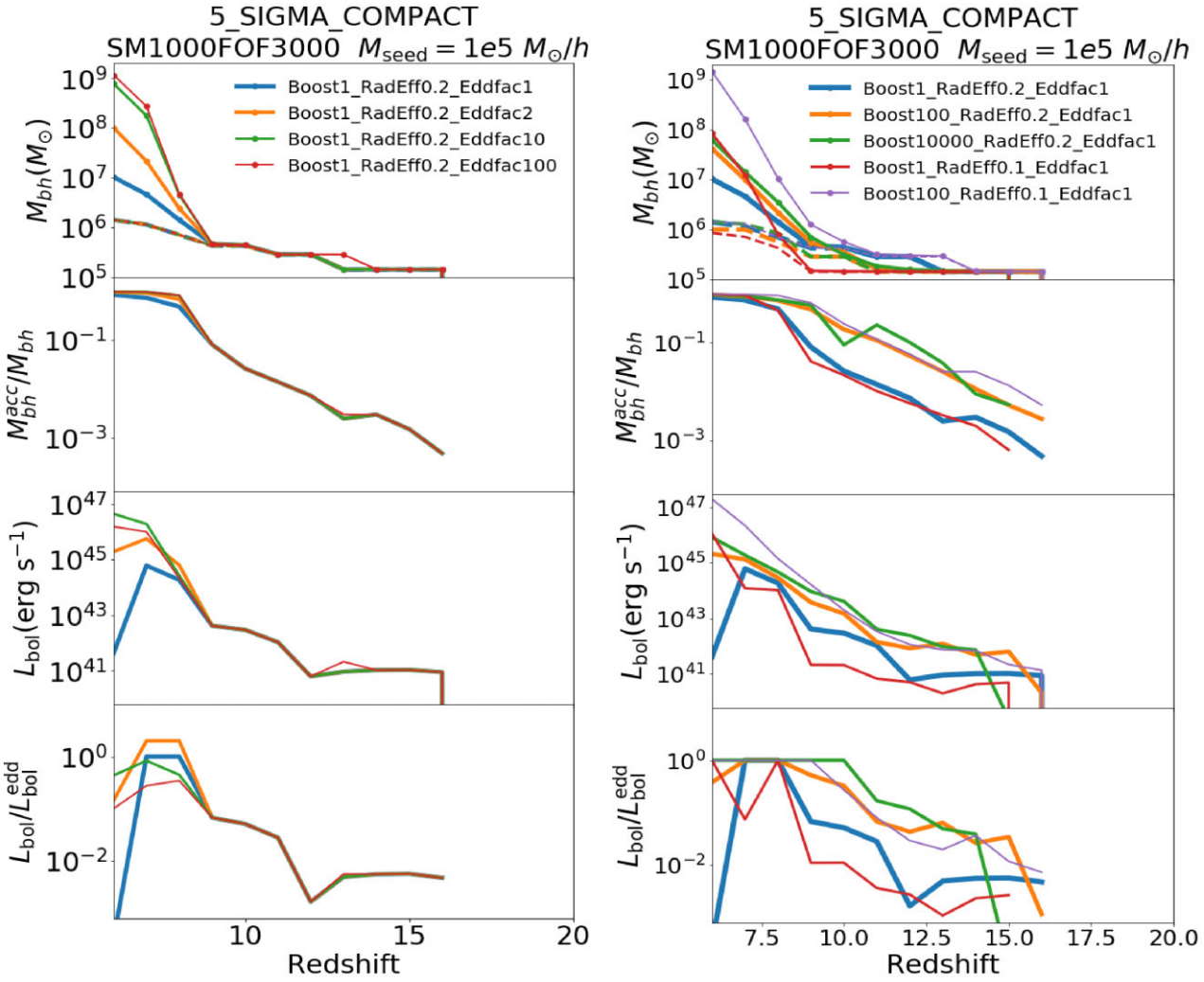

Figure 10. Evolution of the most massive BH in the `5SIGMA_COMPACT` volume for different accretion models labelled hereafter as `Boost*_RadEff*_EddFac*` where the '*'s correspond to values of α, ϵ_r, and $f_{\rm edd}$, respectively. All the runs use the most stringent gas-based seed model `SM1000_FOF3000`, wherein the growth via mergers is small. We then explore different accretion models. In the left-hand panel, we keep $\alpha = 1$ and $\epsilon_r = 0.2$ fixed, and show the BH growth histories for different values of $f_{\rm edd}$ between 1 and 100. In the right-hand panel, we consider different combinations of $\alpha = 1$–$10\,000$ and $\epsilon_r = 0.2$ and 0.1. In the absence or lack of mergers, accretion alone can assemble a 10^9 M$_\odot$ BH at $z \sim 6$ only if we enhance the maximum allowed accretion rate compared to the TNG accretion model. This can be achieved by either allowing for super-Eddington accretion rate, or by reducing the radiative efficiency. In contrast, a higher Bondi boost alone does not sufficiently enhance BH growth to assemble a $z \sim 6$ quasar.

nosity, and Eddington ratio evolution. As we increase $\tilde{M}_{\rm sf,mp}$, fewer seeds form and the merger-driven BH growth is commensurately suppressed. This leads to a significant slow-down of BH growth, and thereby decreases the BH mass assembled by $z = 6$. For 10^5 M$_\odot\,h^{-1}$ seeds, increasing $\tilde{M}_{\rm sf,mp}$ from 5 to 1000 decreases the final $z = 6$ BH mass by a factor of $\sim$100. The $z = 6$ luminosities also drop from $\sim 10^{47}$ to $\sim 10^{43}$ erg s^{-1}. For more massive 8×10^5 M$_\odot\,h^{-1}$ seeds, the impact is significantly stronger (no 8×10^5 M$_\odot\,h^{-1}$ seeds form for $\tilde{M}_{\rm sf,mp} = 1000$). In general, any gas-based seeding prescription that is more restrictive than `SM5_FOF3000` fails to produce BHs consistent with the observed $z \sim 6$ quasars.

Overall, we find that within the TNG galaxy formation model, the `SM5_FOF3000` gas-based seed model is able to successfully reproduce $z \sim 6$ BHs that are comparable to the observed high-z quasars, but only in massive ($\sim 10^{12}$ M$_\odot$) haloes that are highly compact and have low tidal fields. Additionally, both (1) merger-dominated growth at $z \gtrsim 9$, and (2) accretion-dominated growth at $z \sim 6$–9 are crucial for producing these high-z quasars.

3.3 Implications for strongly restrictive seed models in producing $z \gtrsim 6$ quasars

We have thus far seen that $z \sim 6$ quasars cannot be assembled by our constrained simulations without an early boost in BH mass via mergers. This can only occur for relatively less restrictive seed models ($\tilde{M}_{\rm sf,mp} = 5$), wherein enough seeds are formed to substantially contribute to merger-driven BH growth. Here, we look for circumstances under which more restrictive seed models can produce $z \sim 6$ quasars even in the absence of sufficient mergers. In particular, we explore models with enhanced accretion in these highly biased regions, compared to the TNG accretion model.

In Fig. 10, we take one of our most restrictive seeding models i.e. $\tilde{M}_{\rm sf,mp} = 1000$, and explore different accretion models to identify the ones that can produce $z \sim 6$ quasars. As already noted in the previous section, only a handful of seeding and merger events occur for this model. We then investigate the BH growth under different variations for the accretion model. In the left-hand panel, we keep

$\alpha = 1$ and $\epsilon_r = 0.2$ fixed and vary $f_{\rm edd}$ from 1 to 100 (recall that sets the maximum accretion rate in the units of the Eddington rate). Not unexpectedly, we find that as $f_{\rm edd}$ is increased, the final BH mass is enhanced via accretion-driven BH growth. $f_{\rm edd} \gtrsim 10$ is required for growing BHs to $\sim 10^9\,{\rm M}_\odot$ with luminosities $\sim 10^{47}$ erg s^{-1} by $z = 6$ (Fig. 10: green line). Notably, further increasing $f_{\rm edd}$ to 100 does not lead to any substantial increase in the final BH mass beyond $\sim 10^9\,{\rm M}_\odot$ (Fig. 10, right-hand panel: red line). This is because the Bondi accretion rate exceeds 100× the Eddington limit for only a small fraction of the time.

We now keep $f_{\rm edd}$ fixed at 1 and examine the impact of the boost factor α. When α is increased from 1 to 100, it leads to a factor ∼5 increase in the final BH mass at $z = 6$ (blue versus orange lines in Fig. 10: right-hand panel). This is substantially smaller than the impact of increasing $f_{\rm edd}$ to 10. Additionally, further increasing the boost factor to 10 000 (green lines in Fig. 10: right-hand panel) makes no significant difference in the $z = 6$ BH mass. This implies that the maximum accretion rate set by the Eddington factor is much more consequential to the $z = 6$ BH mass, compared to the Bondi boost factor. This is because the majority of the BH mass assembly occurs at $z \lesssim 9$ when the accretion rates are already at their maximum allowed value. To that end, note that the maximum accretion rate can also be increased by decreasing the radiative efficiency ϵ_r. Several cosmological simulations (including N21) use a lower efficiency of $\epsilon_r = 0.1$. If we fix $\alpha = 1$ and decrease the radiative efficiency from 0.2 to 0.1, the $z = 6$ BH mass increases by factor of 10 (see blue versus red lines in Fig. 10: right-hand panel). Not surprisingly, this is similar to what we found when $f_{\rm edd}$ was increased to 2 (revisit Fig. 10: left-hand panel). Notably, at this lower radiative efficiency of $\epsilon_r = 0.1$, applying a boost of $\alpha = 100$ forms a $\sim 10^9\,{\rm M}_\odot$ BH with luminosity of $\sim 10^{47}$ erg s^{-1} at $z = 6$ (purple line in Fig. 10: right-hand panel). This is consistent with the results of N21, as we shall see in more detail in Section 3.8.

To summarize our results thus far, we have shown that to form the observed $z \sim 6$ quasars within rare dense compact haloes in our simulations, one of the following two requirements must be fulfilled:

(i) When the default TNG model is used (i.e. $\alpha = 1, \epsilon_r = 0.2$, and $f_{\rm edd} = 1$), we need a sufficiently early ($z \gtrsim 9$) boost in BH mass driven by BH mergers to grow to $\sim 10^9\,{\rm M}_\odot$ by $z = 6$. Our gas-based seeding prescription with $\tilde{M}_{\rm sf,mp} = 5$ and $\tilde{M}_h = 3000$ satisfies this requirement.

(ii) For more restrictive seeding models ($\tilde{M}_{\rm sf,mp} \gtrsim 150$) where mergers are absent or insufficient, $z \sim 6$ quasars cannot be produced unless we enhance the maximum allowed accretion rate (by factors $\gtrsim 10$) within these extreme overdense regions by either increasing the Eddington factor or decreasing the radiative efficiency. Notably, this result is consistent with the recent work of Hu et al. (2022) who use semi-analytic approach to produce $z \sim 6$ quasars using super-Eddington accretion, from both light ($10\,{\rm M}_\odot$) and heavy seeds ($10^5\,{\rm M}_\odot$).

3.4 Impact of seed model on BH growth for 'growth optimized' accretion parameters

Given that some of these BH accretion models can produce massive BHs by $z \sim 6$ without an early boost from BH mergers, we now explore what happens when these 'growth optimized' accretion parameters are combined with merger-driven growth from less restrictive BH seed models. In the left-hand panel of Fig. 11, we take the accretion model $\alpha = 1, \epsilon_r = 0.2$, and $f_{\rm edd} = 10$, and compare the BH growth histories for two seed models with $\tilde{M}_{\rm sf,mp} =$

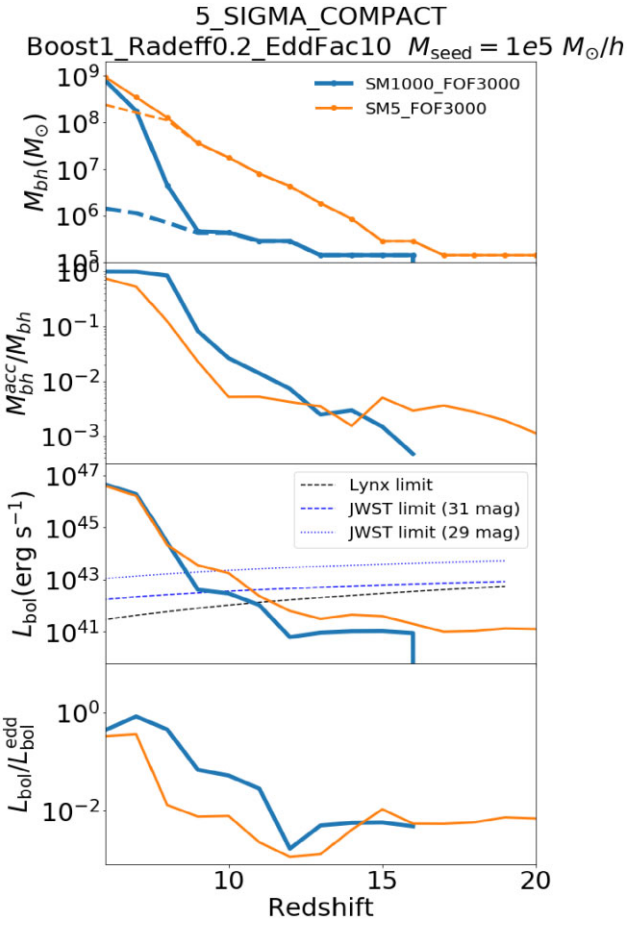

Figure 11. Here, we consider the model `Boost1_Radeff0.2_Eddfac10` that can already grow a $z \sim 6$ quasar via accretion alone, and then investigate the impact of enhancing the number of seeds and mergers on the final BH mass at $z = 6$. The blue lines correspond to $\tilde{M}_{\rm sf,mp} = 1000$ (`SM1000_FOF3000`), which does not produce many seeds and mergers. The orange lines correspond to $\tilde{M}_{\rm sf,mp} = 5$ (`SM5_FOF3000`) which does produce a substantial number of seeds and mergers. We find that in models such as `Boost1_Radeff0.2_Eddfac10` wherein BHs can already grow to $\sim 10^9\,{\rm M}_\odot$ via accretion alone, introducing more seeds and mergers (by reducing $\tilde{M}_{\rm sf,mp}$), does not lead to any further increase in the final BH mass at $z = 6$. In the third panel, the black dashed line is the detection limit of 10^{-19} erg cm^{-2} s^{-1} of the Lynx 2–10 keV band, derived using bolometric corrections adopted from Vasudevan & Fabian (2007). The blue dashed and dotted lines are *JWST* detection limits of 31th and 29th apparent magnitude for exposure times of 10^5 and 10^4 s, respectively (same as those assumed in Vogelsberger et al. 2020b), with bolometric correction adopted from Elvis et al. (1994). Therefore, *JWST* and Lynx observations of the quasar progenitors at $z \sim 9$–10 could potentially contain signatures of their seeding environments.

5 and 1000 (`SM5_FOF3000` and `SM1000_FOF3000`, respectively). We have already seen that `SM1000_FOF3000` produces a $\sim 10^9\,{\rm M}_\odot$ BH with $\sim 10^{47}$ erg s^{-1} luminosity at $z = 6$ even in the absence of significant number of mergers. We now examine whether the substantial merger-driven growth of `SM5_FOF3000` leads to any further increase in the $z = 6$ BH mass much beyond $\sim 10^9\,{\rm M}_\odot$, when combined with super-Eddington accretion of $f_{\rm edd} = 10$. The `SM5_FOF3000` model grows BHs via mergers to $\sim 10^7\,{\rm M}_\odot$ by $z \sim 9$, which is a factor of ∼500 higher than the `SM1000_FOF3000` model. Despite this large difference in masses, the luminosities are similar in both models, such that the higher-mass BH in `SM5_FOF3000` has

a lower Eddington ratio. By $z = 6$, the BH in SM5_FOF3000 reaches a mass of $\sim 10^9$ M$_\odot$, similar to SM1000_FOF3000. To summarize, if a given model is already producing a $\sim 10^9$ M$_\odot$ BH at $z \sim 6$ via accretion alone, boosting the merger-driven BH growth by forming more seeds does not further increase the final $z = 6$ BH mass by a significant amount.

The results from Fig. 11 also imply that if the accretion model is such that $z \sim 6$ quasars can be assembled via accretion alone, multiple sets of seed models can produce the observed $z \sim 6$ quasars. In such a case, the $z \sim 6$ quasar observations alone may not be able to constrain BH seed models. However, the progenitors of these quasars at $z \gtrsim 9$ can have significantly different assembly histories depending on the seed model, particularly in terms of the contribution from BH mergers. In fact, SM5_FOF3000 naturally predicts a $\sim$100 times higher number of mergers compared to SM1000_FOF3000. Moreover, these merging progenitors will likely include the most massive BHs at their respective redshift. Therefore, detection of the loudest LISA events at $z \gtrsim 9$ are likely to provide strong constraints for seed models. In terms of electromagnetic observations, the AGN progenitors are above of the detection limits of Lynx and *JWST* (with limiting apparent magnitude of 31) up to $z \sim 10$; this is true for both SM5_FOF3000 and SM1000_FOF3000 models (revisit the third row of Fig. 11). However, the difference in luminosities produced by both seed models is within a factor of $\sim$10, corresponding to a magnitude difference of only $\sim$2.5. Therefore, it is likely going to be difficult to find imprints of seed models within Lynx and *JWST* observations of the brightest AGNs at higher redshifts ($z \gtrsim 9$).

3.5 BH growth at higher resolutions

We have thus far presented results at our fiducial resolution of $N = 360$, corresponding to gas mass resolution of $\sim 10^5$ M$_\odot\, h^{-1}$. While we were able explore a wide range of models at this resolution at reasonable computational cost, we demonstrated in Bhowmick et al. (2021b) that our gas-based seed models start to become reasonably well converged only at resolutions $\lesssim 10^4$ M$_\odot\, h^{-1}$. Therefore, it is imperative to perform a resolution convergence test by running some of these simulations at gas mass resolutions of $\sim 10^4$ M$_\odot\, h^{-1}$ ($N = 720$). Particularly, we consider the seed models SM5_FOF3000 with $\alpha = 1$, $\epsilon_r = 0.2$, $f_{\rm edd} = 1$, and SM1000_FOF3000 with $\alpha = 1$, $\epsilon_r = 0.2, f_{\rm edd} = 10$, both of which successfully produced a $\sim 10^9$ M$_\odot$ quasar by $z \sim 6$. Due to computational reasons, we could only run the higher resolution simulations ($N = 720$) to $z = 7$.

The results are shown in Fig. 12, where they are compared to the lower resolution runs ($N = 360$). Let us start with SM5_FOF3000 (left-hand panels), which produces enough seeds to allow for substantial amounts of merger-driven BH growth. The number of seeds formed (Fig. 12: top left-hand panel) is similar between $N = 360$ and 720 for $z \gtrsim 12$. As shown in Bhowmick et al. (2021b), at these redshifts, seeding is largely driven by the proliferation of new star-forming regions (star formation is reasonably well converged between gas mass resolutions of $\lesssim 10^5$ M$_\odot\, h^{-1}$). At $z \lesssim 12$, the higher resolution simulation produces a somewhat lower number of seeds (by factors up to $\sim$5). The slower resolution convergence at $z \sim$ 7–12 is also fully consistent with the zoom simulations of Bhowmick et al. (2021b). It is due to the markedly stronger metal dispersion for higher resolutions, which causes a stronger suppression of seeding at $z \sim$ 7–12 relative to lower resolution simulations. Nevertheless, the final $z = 7$ BH mass of $\sim 10^8$ M$_\odot\, h^{-1}$ assembled by the higher resolution simulation (Fig. 12: bottom left panel) is only slightly smaller (by a factor of $\sim$1.5) compared to the lower resolution simulation. This strongly indicates at even at higher resolutions, the

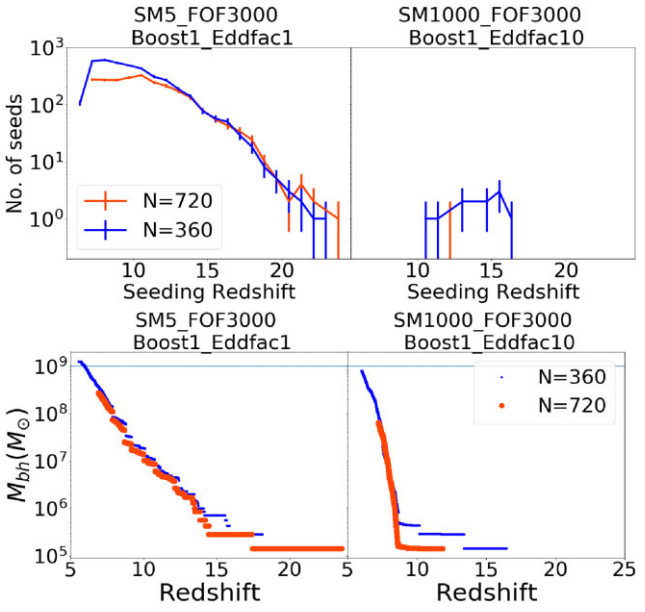

Figure 12. The top and bottom panels show the total number of seeds formed and growth of the most massive BH, respectively, for $M_{\rm seed} = 10^5$ M$_\odot\, h^{-1}$ at two different resolutions, namely $N = 360$ and $N = 720$. We show the resolution convergence for two distinct seed models which produce a $\sim 10^9$ M$_\odot$ BH by $z = 6$. The left-hand panels correspond to the least restrictive seeding model of $\tilde{M}_{\rm sf,mp} = 5$, $\tilde{M}_{\rm h} = 3000$, wherein mergers substantially dominate the growth at $z \gtrsim 9$ and accretion model is Eddington limited with $\alpha = 1$, $\epsilon_r = 0.2$, $f_{\rm edd} = 1$. The right-hand panels correspond to the much more restrictive seed model of $\tilde{M}_{\rm sf,mp} = 1000$, $\tilde{M}_{\rm h} = 3000$ with insignificant merger-driven growth; the accretion model corresponds to $\alpha = 1$, $\epsilon_r = 0.2$, $f_{\rm edd} = 10$. In both the seed models, the final BH masses at $z \sim 7$ are similar for $N = 360$ and $N = 720$.

SM5_FOF3000 seed model would be able to assemble a $\sim 10^9$ M$_\odot$ by $z = 6$.

Now let us focus on the SM1000_FOF3000 model (with $f_{\rm edd} = 10$), where the merger-driven BH growth is minimal and super-Eddington growth is used to produce a $\sim 10^9$ M$_\odot$ by $z = 6$. Here, the higher resolution run ($N = 720$) produces only 1 seed, whereas the lower resolution produced $\sim$10 seeds (Fig. 12: top right-hand panel). This is also consistent with our findings in Bhowmick et al. (2021b) where we showed that resolution convergence becomes poorer as seed models become more restrictive with higher $\tilde{M}_{\rm sf,mp}$. Despite this, the accretion-driven BH growth at $z \lesssim 9$ assembles a BH mass close to $\sim 10^8$ M$_\odot$ by $z \sim 7$ for both $N = 720$ and 360 resolutions (Fig. 12: bottom right-hand panel). Overall, we find that the BH models which successfully produce a $z \gtrsim 6$ quasar at our fiducial resolution ($N = 360$) will likely continue to do so at even higher resolutions.

3.6 DCBHs as possible seeds of $z \gtrsim 7$ quasars

Here, we use the higher resolution simulations ($N = 720$) to investigate the possibility of DCBHs as candidates for the seeds of the $z \gtrsim 6$ quasars. The conditions for their formation are very restrictive due to the requirement of high LW flux incident upon dense, pristine gas. In particular, small-scale hydrodynamic simulations (Shang et al. 2010) and one-zone chemistry models (Sugimura et al. 2014; Wolcott-Green et al. 2017) infer critical LW fluxes to be $\gtrsim 10^3$ J_{21}. In the zoom simulations of Bhowmick et al. (2021a) that contained a 3.3σ overdense peak (for a target halo mass of 3.5×10^{11} M$_\odot\, h^{-1}$ at $z = 5$), the highest LW flux incident within dense, metal-poor gas

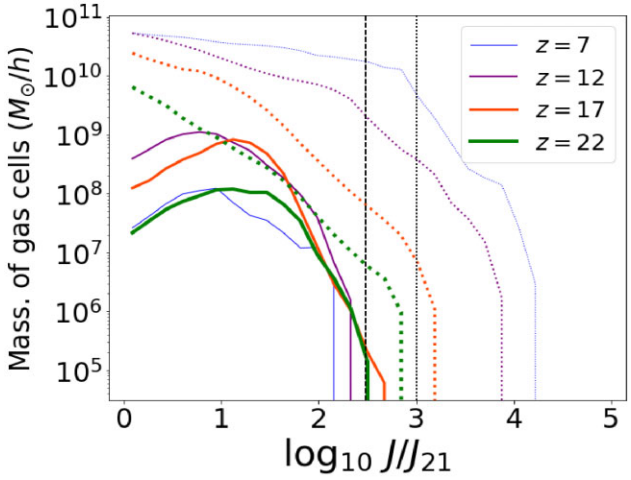

Figure 13. Total mass of gas cells illuminated by LW photons within bins of various flux values shown in the *x*-axis. These are runs at $N = 720$ (higher than the fiducial resolution). The dotted lines correspond to all gas cells and solid lines correspond to dense, metal-poor gas cells. The black vertical lines correspond to flux thresholds of $J_{\rm crit} = 300\ J_{21}$ (dashed) and $J_{\rm crit} = 1000\ J_{21}$ (dashed). When we look at all gas cells, flux values can reach up to $\sim 10^4\ J_{21}$. However, within dense, metal-poor regions, flux values reach only up to $\sim 300\ J_{21}$. Therefore, for DCBHs seeds to form in our constrained regions, the critical LW flux values need to be less than $\sim 300\ J_{21}$. One-zone chemistry models and high-resolution hydrodynamic simulations predict significantly higher critical flux ($\gtrsim 1000\ J_{21}$).

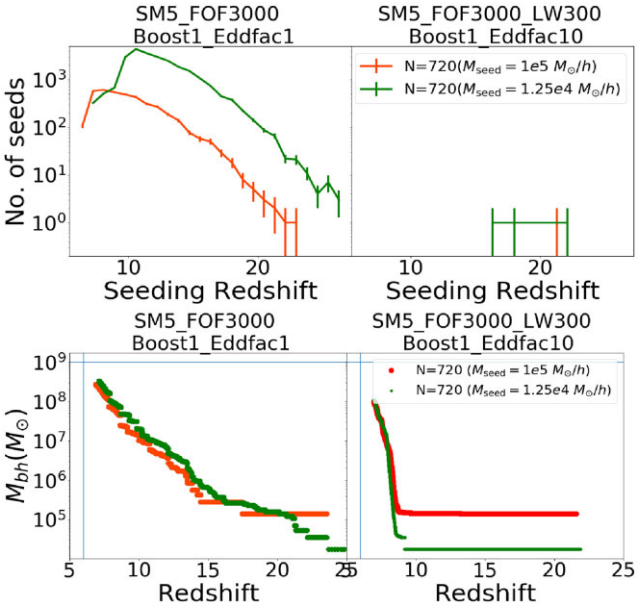

Figure 14. The top and bottom panels, respectively, show the number of seeds and BH mass growth at $N = 720$ for two different seed masses of $M_{\rm seed} = 10^5$ and $1.25 \times 10^4\ {\rm M}_\odot\ h^{-1}$. The left-hand panels correspond to the least restrictive seeding model of $\tilde{M}_{\rm sf,mp} = 5$, $\tilde{M}_{\rm h} = 3000$, wherein mergers substantially dominate the growth at $z \gtrsim 9$ and accretion rate is Eddington limited. Here, $1.25 \times 10^4\ {\rm M}_\odot\ h^{-1}$ seeds form and merge ~ 8 times more frequently than $1 \times 10^5\ {\rm M}_\odot\ h^{-1}$ seeds. Both seed masses grow to similar mass BHs by $z \sim 7$. The right-hand panels correspond to the much more restrictive seed model of $\tilde{M}_{\rm sf,mp} = 5$, $\tilde{M}_{\rm h} = 3000$ and critical LW flux of $300\ J_{21}$; the accretion model is given by $\alpha = 1$, $\epsilon_r = 0.2, f_{\rm edd} = 10$. Here, the merger-driven growth is insignificant. Regardless, both seed masses produce similar mass BHs by $z \sim 7$.

was $\sim 100\ J_{21}$. The work showed that the bulk of the $z \gtrsim 6$ SMBH population may be difficult to explain via the DCBH seeding channel.

We investigate whether DCBHs can form in the `5SIGMA_COMPACT` region, which is much more extreme compared to the region probed in Bhowmick et al. (2021a). Fig. 13 shows the distribution of LW intensities at various redshifts, across all gas cells (dotted lines) as well as dense, metal-poor gas cells (solid lines). In general, the LW intensities can be as high as $\sim 10^4\ J_{21}$. However, when we exclusively look at dense, metal-poor gas, the LW intensities span only up to $\sim 300\ J_{21}$. When we apply a critical flux threshold of $\sim 300\ J_{21}$ for seeding (`SM5_FOF3000_LW300`), only a handful of seeds are formed (Fig. 14: upper right-hand panel). For higher critical fluxes e.g. $\sim 10^3\ J_{21}$, there is no DCBH seed formation. Therefore, our model can support DCBHs as potential candidates for the seeds of $z \gtrsim 6$ quasars only if the critical LW flux is $\lesssim 300\ J_{21}$. Secondly, due to the absence of any significant merger-driven BH growth, to produce $z \sim 6$ quasars from these very few DCBH seeds, we need to enhance the maximum allowed accretion rate compared to the TNG accretion model by allowing for super-Eddington accretion or reducing the radiative efficiency (as follows from the results of Section 3.3). As an example, the lower right-hand panel of Fig. 14 shows the growth of a DCBH seed ($J_{\rm crit} = 300\ J_{21}$) to $\sim 10^8\ {\rm M}_\odot\ h^{-1}$ by $z = 7$ via super-Eddington accretion with $f_{\rm edd} = 10$. Given the trends from the lower resolution $N = 360$ simulations, we expect the BH to continue growing to $\sim 10^9\ {\rm M}_\odot$ by $z = 6$.

Lastly, while the LW criterion is very restrictive to DCBH seed formation in our simulations, recall that there are several possible scenarios under which DCBHs could form even in the absence or lack of LW radiation. These include suppression of H_2 via collisional dissociation or trapping of Lyman α by neutral Hydrogen (Spaans & Silk 2006; Schleicher et al. 2010; Latif et al. 2011; Inayoshi & Omukai 2012), supersonic streaming of baryons (Tanaka & Li 2014; Hirano et al. 2017; Schauer et al. 2019), dynamical heating during rapid growth of massive haloes (Fernandez et al. 2014; Wise et al. 2019; Regan et al. 2020) (see also Section 1 for more details). Inclusion of these scenarios may lead to higher number of DCBHs in our constrained regions. We shall investigate this in future work.

3.7 Impact of seed mass on the formation of $z \gtrsim 6$ quasars

At our fiducial resolution ($N = 360$), we were able to probe seed masses of 10^5 and $8 \times 10^5\ {\rm M}_\odot\ h^{-1}$. The higher resolution simulations ($N = 720$) allow us to probe seed masses down to $\sim 10^4\ {\rm M}_\odot$. In Fig. 14, we reduce the seed mass from 10^5 to $1.25 \times 10^4\ {\rm M}_\odot\ h^{-1}$ and study its impact on the final BH mass at $z = 7$. We again consider two models that have been shown to successfully produce a $\sim 10^9\ {\rm M}_\odot\ h^{-1}$ at $z \sim 6$. We start with the `SM5_FOF3000` model (left-hand panels) where there is substantial amount of merger-driven BH growth. Here, we see that the $1.25 \times 10^4\ {\rm M}_\odot\ h^{-1}$ seeds form ~ 8 times more abundantly compared to $1 \times 10^5\ {\rm M}_\odot\ h^{-1}$ seeds. As a result, $1.25 \times 10^4\ {\rm M}_\odot\ h^{-1}$ seeds undergo more mergers and grow to similar masses as $1 \times 10^5\ {\rm M}_\odot\ h^{-1}$ seeds by $z \sim 7$ (as also seen in Bhowmick et al. 2021b). At $z = 7$, both the seed masses assemble a $\sim 10^8\ {\rm M}_\odot$ BH.

Next, we consider the model `SM5_FOF3000_LW300` which adds an LW flux criterion with $J_{\rm crit} = 300\ J_{21}$. This model (as seen in the previous section) is so restrictive that only a handful of seeds are formed in the entire simulation box (Fig. 14: top right-hand panel). Here, we allow for super-Eddington accretion with $f_{\rm edd} = 10$ (see Fig. 14: bottom right-hand panel). We can see that for $M_{\rm seed} = 10^5\ {\rm M}_\odot\ h^{-1}$, there are no mergers in its history; and

for $M_{\rm seed} = 1.25 \times 10^4\,{\rm M}_\odot\,h^{-1}$, there is only one merger. In the absence of mergers, there is no appreciable growth of these seeds at $z \gtrsim 9$. Despite that, both 10^5 and $1.25 \times 10^4\,{\rm M}_\odot\,h^{-1}$ seeds grow to $\sim 10^8\,{\rm M}_\odot\,h^{-1}$ via accretion between $z \sim 9$ and 7.

To summarize, whether we consider models where $z \sim 6$ quasars are formed either with the help of BH mergers, or gas accretion alone, the mass assembled at $z \sim 6$–9 is not sensitive to the seed mass in the range 10^4–$10^6\,{\rm M}_\odot\,h^{-1}$. Note however that we are not able to probe seed masses below $\sim 10^4\,{\rm M}_\odot$ due to resolution limitations. It is possible that these lowest mass seeds ($\sim 10^2$–$10^3\,{\rm M}_\odot$) may not be able to grow into the $z \gtrsim 6$ quasars, particularly in the absence or lack of mergers; we shall investigate this in future studies.

3.8 Comparison with other theoretical works

Here, we compare our results to other theoretical works that have explored the formation of the $z \gtrsim 6$ quasars. We will first compare with hydrodynamic simulations, where we note that most of the existing work has so far used seed models that are only based on halo mass. Our simulations using the TNG seed model therefore provide the most direct comparison to such studies. We start with the constrained simulations of N21 produced using the MP-GADGET code (Feng et al. 2018) with the BlueTides galaxy formation model (Feng et al. 2016). Their primary constrained peak (referred to as BIG-BH in their work) is very similar to 5SIGMA_COMPACT. Their seed model is also similar to the TNG seed model; they adopt the same halo mass threshold for seeding ($> 5 \times 10^{10}\,{\rm M}_\odot\,h^{-1}$), but with a slightly smaller seed mass of $5 \times 10^5\,{\rm M}_\odot\,h^{-1}$. Notably, their simulation produced a $\sim 3 \times 10^8\,{\rm M}_\odot$ BH by $z = 7$, which is significantly higher than the predictions in our simulations with the TNG seeding and accretion model. But N21 uses a lower radiative efficiency of $\epsilon_r = 0.1$ and a Bondi boost factor of $\alpha = 100$, which we have already shown to produce a much stronger growth compared to the TNG accretion model (revisit Fig. 10: right-hand panel). Additionally, they also have a higher Eddington factor of $f_{\rm edd} = 2$.

We perform a more direct comparison to N21 in Fig. 15 by simulating a box identical to their work, particularly in terms of volume (20 Mpc h^{-1} box length), resolution ($N = 352$), initial condition (BIG-BH), and the BH seed model ($5 \times 10^5\,{\rm M}_\odot\,h^{-1}$ seeds in $> 5 \times 10^{10}\,{\rm M}_\odot\,h^{-1}$ haloes). If we apply the TNG accretion model ($\alpha = 1, f_{\rm edd} = 1, \epsilon_r = 0.2$), our BIG-BH simulation assembles a BH of mass $\sim 10^7\,{\rm M}_\odot$ by $z = 7$ (Fig. 15: purple line); this is ∼30 times smaller than the N21 predictions (similar to that of 5SIGMA_COMPACT). Next, if we individually adjust each of these accretion parameters (Fig. 15: pink, green, and blue lines) to the N21 values (one parameter at a time), we find that they all lead to notable enhancement in the BH growth (as also seen in Section 3.3 for SM1000_FOF3000). Finally, if all the accretion parameters in our simulations are simultaneously set to be the same as N21 (Fig. 15: black line), we produce a $\sim 5 \times 10^8\,{\rm M}_\odot$ BH by $z = 7$, which is only slightly higher than the N21 predictions. Overall, our results are broadly consistent with N21. The same general conclusion also applies to the comparison with the results of Huang et al. (2020), which performs constrained runs using MP-GADGET similar to that of N21. Notably, they find that the final mass at $z \sim 6$ is insensitive to the seed mass for $\sim 5 \times 10^4$–$5 \times 10^5\,{\rm M}_\odot\,h^{-1}$ seeds, which is consistent with our findings.

The zoom simulations of Sijacki et al. (2009), Feng et al. (2014), and Costa et al. (2014) adopted a Bondi boost factor of 100 and radiative efficiencies of 0.05–0.1; with this accretion model, they successfully produced the $z \sim 6$ quasars without the need for mergers

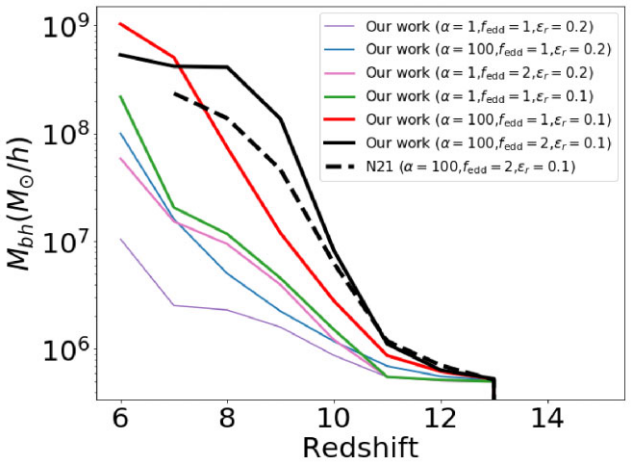

Figure 15. Comparison between the BH growth histories for the constrained runs in our work versus Ni et al. (2021) (hereafter N21). Their simulations were run using the MP-GADGET code (Feng et al. 2018) with the galaxy formation model adopted from the BlueTides simulation (Feng et al. 2016). The solid lines show predictions from our simulations, and the dashed line is the prediction from N21. To make a fair comparison, we tune our simulation box, initial conditions to be the same as that used in N21 (box size of 20 Mpc h^{-1} with $N = 352$). We also use the same 'halo-mass-based' seeding prescription as N21, with $5 \times 10^5\,{\rm M}_\odot\,h^{-1}$ seeds placed inside $> 5 \times 10^{10}\,{\rm M}_\odot\,h^{-1}$ haloes. Our fiducial model (with $\alpha = 1, f_{\rm edd} = 1, \epsilon_r = 0.2$) assembles a significantly lower BH mass (by factors of ∼30) compared to N21. This difference is due to the combined effect of the higher Bondi boost factor and Eddington factor, as well as lower radiative efficiency used in N21. In fact, when we use the same accretion parameters as N21 ($\alpha = 100$, $f_{\rm edd} = 2$, $\epsilon_r = 0.1$), we produce a slightly higher (by factor of ∼2) mass BH compared to their work.

or super-Eddington accretion, consistent with our results. Zhu et al. (2020) performed zoom simulations targeting the formation of a $\sim 10^{13}\,{\rm M}_\odot$ halo at $z = 6$. In their fiducial model, they placed $10^5\,{\rm M}_\odot/h$ seeds in $10^{10}\,{\rm M}_\odot/h$ haloes. These seeds grew via Eddington limited Bondi accretion ($\alpha = 1, f_{\rm edd} = 1$) with radiative efficiency of $\epsilon_r = 0.1$. With this model, they were able to grow a $\sim 10^9\,{\rm M}_\odot$ BH by $z = 6$ without the help of substantial merger-driven BH growth, super-Eddington accretion, or a Bondi boost. They achieve somewhat faster BH growth compared to our simulations, which only assembles a $\sim 2 \times 10^8\,{\rm M}_\odot$ BH by $z = 6$ if $\epsilon_r = 0.1$ is applied without a Bondi boost (see green line in Fig. 15). While it is not clear what may be causing the difference between our results and Zhu et al. (2020), it may be attributed to differences in the implementation of other aspects of the galaxy formation model such as metal enrichment and stellar feedback. However, when they increased their radiative efficiency to 0.2, their final BH mass at $z = 6$ dramatically decreased to $\sim 4 \times 10^7\,{\rm M}_\odot$, consistent with our findings. Finally, early work by Li et al. (2007) also produced a $\sim 10^9\,{\rm M}_\odot$ quasar with $\epsilon_r = 0.1$ and $\alpha = 1$, $f_{\rm edd} = 1$ within a $8 \times 10^{12}\,{\rm M}_\odot$ halo at $z = 6.5$. Notably, their host halo was assembled after a series of eight major mergers between $z \sim 14$ and 6.5. Their results therefore highlighted yet another formation pathway for high-z quasars i.e. via a series of intermittent rapid growths driven by major mergers.

Similar to Zhu et al. (2020), Lupi et al. (2019) was also able to produce a $\sim 10^9\,{\rm M}_\odot$ by $z \sim 6$ with Eddington limited Bondi accretion and radiative efficiency of 0.1, without applying a Bondi boost factor. This may be due to their adopted thermal feedback efficiency of 0.005, which is significantly smaller than values (∼0.05–0.15) adopted for most other works including ours. The very recent work of

Valentini, Gallerani & Ferrara (2021) considered even lower radiative efficiencies of 0.03, allowing them to grow BHs to $\sim 10^9$ M$_\odot$ by $z \sim 6$ via feedback regulated Bondi accretion without the need of a Bondi boost factor. Lastly, Radiation hydrodynamics zoom simulations of Smidt et al. (2018) also adopted a radiative efficiency of 0.1 and is able to assemble a $\sim 10^9$ M$_\odot$ BH by $z \sim 7$ despite gas accretion being sub-Eddington (and no substantial contribution from BH mergers) for almost the entire growth history; however it is difficult to compare their results to our work since they adopted the alpha disc formalism (see equation 2 of Debuhr et al. 2010) to calculate the BH accretion rate, where there is no explicit dependence on BH mass.

While previous hydrodynamic simulations probing $z \gtrsim 6$ quasars have mostly adopted halo-mass-based prescriptions for seeding, SAMs have been able to explore a broader range of seeding channels (and seed masses) with more physically motivated seeding criterias (for example, Sesana et al. 2007; Volonteri & Natarajan 2009; Barausse 2012; Ricarte & Natarajan 2018; Valiante et al. 2018; Dayal et al. 2019; DeGraf & Sijacki 2020). Here, we shall compare with works that have used SAMs to make predictions specific to the $z \gtrsim 6$ quasars. Valiante et al. (2016) and Sassano et al. (2021) used the GAMETE/QSOdust data constrained SAM (introduced in Valiante et al. 2016) to trace the formation of a $\sim 10^9$ M$_\odot$ BH along the merger tree of a 10^{13} M$_\odot\, h^{-1}$ halo at $z = 6.42$. They find that heavy seeds ($\sim 10^5$ M$_\odot\, h^{-1}$) contribute the most to the formation of $z \gtrsim 6$ quasars compared to light ($\sim 10^2$ M$_\odot\, h^{-1}$) and intermediate seeds ($\sim 10^3$ M$_\odot\, h^{-1}$). While we cannot probe light and intermediate seeds, their results for the heavy seeds do not conflict with our findings. They also apply a radiative efficiency of 0.1 combined with a Bondi boost factor of 50–150, and are able to assemble $z \sim 6$ quasars without substantial contributions from BH mergers or super-Eddington accretion. This is fully consistent with our results, and also with results from other hydrodynamic simulations.

Overall, we find that the differences between our results with IllustrisTNG physics and the results from most previous works are largely originating from differences in the modelling of BH accretion and feedback. This also brings to light that when the default IllustrisTNG physics is applied to such extreme overdense regions, it is much more difficult to form $z \sim 6$ quasars compared to the physics adopted in other simulations and SAMs. This is primarily due to the TNG accretion model which has a higher radiative efficiency of 0.2 (most works adopt a value of 0.1). At the same time, the lack of a Bondi boost also slows the BH growth even further (most works adopted a value of 100) in the TNG accretion model. Note that the uncertainties within the modelling of BH accretion are significant, particularly at high redshifts wherein the gas environments are likely to be very different compared to the assumptions underlying the Bondi accretion model. Additionally, the radiative efficiencies are also poorly constrained. To that end, different subgrid models are better or worse at reproducing different aspects of the observed SMBH and galaxy populations (e.g. Habouzit et al. 2021, 2022b). Moving forward, it will be necessary to build better subgrid models with fewer modelling uncertainties, as well as improving the observational constraints particularly on high-z SMBHs.

4 DISCUSSION AND CONCLUSIONS

In this work, we have studied the implications of the IllustrisTNG galaxy formation model on the brightest $z \gtrsim 6$ quasar population, particularly in the context of different BH seeding models. These extremely rare ($\sim$1 Gpc^{-3}) objects have grown to masses of $\sim 10^9$–10^{10} M$_\odot$ (comparable to the most massive $z \sim 0$ SMBHs) within the first Gyr since the big bang; this is difficult to achieve in general, and it is likely to place strong constraints on models for BH formation and growth.

We explore the following seeding prescriptions:

(i) TNG seed model: This is the default 'halo-mass-based' prescription used within the IllustrisTNG simulation suite, where we place 8×10^5 M$_\odot\, h^{-1}$ seeds in $> 5 \times 10^{10}$ M$_\odot\, h^{-1}$ haloes.

(ii) gas-based seed models: Here, we place seeds ($M_{\rm seed} = 1.25 \times 10^4$, 1×10^5, and 8×10^5 M$_\odot\, h^{-1}$) in haloes that exceed critical thresholds for halo mass and dense, metal-poor gas mass (represented by $\tilde{M}_h$ and $\tilde{M}_{\rm sf,mp}$, respectively, in the units of $M_{\rm seed}$). We also explore models where the dense, metal-poor gas is required to have LW fluxes above a critical value $J_{\rm crit}$.

With the above seeding prescriptions, we probe the possible formation of the $z \sim 6$ quasars (defined as $\sim 10^9$ M$_\odot$ BHs with luminosities of $\sim 10^{47}$ erg s^{-1}) within extremely rare peaks in the density field using the technique of constrained Gaussian realizations. This technique allows us to constrain the peak of the density field so as to assemble $\gtrsim 10^{12}$ M$_\odot\, h^{-1}$ haloes by $z \sim 7$ within a simulation volume of (9 Mpc h^{-1})^3. Having a relatively small simulation volume allows us to build a large simulation suite exploring a variety of density peak parameters as well as seeding parameters.

We reproduce findings from previous work (N21) showing that BH growth is most efficient at density peaks that have high compactness and a low tidal field. In fact, a highly compact 5σ peak at 1.0 Mpc h^{-1} with low tidal field (5SIGMA_COMPACT) produces a more massive BH (by factors of $\sim$2) compared to a typical 6σ peak at 1.3 Mpc h^{-1} (6SIGMA). The reason for this is twofold: First, the target $z = 7$ halo in 5SIGMA_COMPACT has more massive progenitors than that of 6SIGMA, allowing seeds to form in potentially higher numbers and boosting the merger-driven BH growth. Second, the 5SIGMA_COMPACT region forms a more compact gas cloud which falls towards the BH more symmetrically from all directions compared to 6SIGMA; this leads to higher gas densities in their neighbourhood and boosts the accretion-driven BH growth.

Despite the enhanced accretion and merger-driven BH growth in 5SIGMA_COMPACT, we find that when the TNG seed model is used, the final mass of the central BH in the target halo at $z = 6$ is only $\sim 5 \times 10^7$ M$_\odot$ with luminosities of $\sim 10^{45}$ erg s^{-1}. This significantly falls short of producing an observed $z \sim 6$ quasar i.e. a $\sim 10^9$ M$_\odot$ BH with a bolometric luminosity of $\sim 10^{47}$ erg s^{-1}. But when we apply the more physically motivated gas-based seeding prescription where BHs are seeded in haloes with minimum star-forming metal-poor gas mass of five times the seed mass and a total halo mass of 3000 times the seed mass ($\tilde{M}_{\rm sf,mp} = 5$ and $\tilde{M}_{\rm h} = 3000$), we find that there is substantial amount of the merger-driven BH growth at $z \gtrsim 10$ compared to the TNG seed model. As a result, the BH assembles a mass of $\sim 10^9$ M$_\odot$ at $z = 6$ and grows close to the Eddington limit with a bolometric luminosity of $\sim 10^{47}$ erg s^{-1}. This is consistent with the observed $z \sim 6$ quasars, and is achievable for all seed mass values in the range $\sim 10^4$–10^6 M$_\odot\, h^{-1}$. Lastly, note that this can also be achieved by enhancing merger-driven growth within halo-mass-based seed models (like TNG seed model) by sufficiently reducing the halo mass threshold.

Notably, there are two distinct phases in the BH growth in our simulations: (1) $z \gtrsim 9$ when the BH growth is predominantly driven by BH mergers, and (2) $z \sim$ 9–6 when gas accretion dominates the BH growth. To form a $z \gtrsim 6$ quasar within a universe with IllustrisTNG physics, the BH growth has to be boosted by BH mergers at $z \gtrsim 9$. Amongst all the seed models we explored, only the one with $\tilde{M}_{\rm sf,mp} = 5$ and $\tilde{M}_{\rm h} = 3000$ provides enough mergers to assemble $z \sim 6$ quasars.

For much more restrictive gas-based seed models ($\tilde{M}_{\rm sf,mp} = 1000$ and $\tilde{M}_{\rm h} = 3000$, for example), very few seeds are formed and there is little to no merger-driven growth; as a result, they fail to produce $z \sim 6$ quasars in the IllustrisTNG universe. However, recall that the IllustrisTNG model was calibrated to reproduce properties of relatively common galaxies and BHs at low redshifts. We explored the possibility of enhanced accretion in these extreme overdense regions compared to the TNG accretion model. We found that in order to form $z \sim 6$ quasars with these restrictive seed models, it is crucial to increase the maximum accretion rate (by factors $\gtrsim 10$) allowed for a BH of a given mass to grow. This can be achieved by either increasing the Eddington factor or decreasing the radiative efficiency. To that end, increasing the Bondi boost factor alone does not sufficiently boost the BH mass assembly to produce the $z \sim 6$ quasars. Lastly, note that even for such high values of $\tilde{M}_{\rm sf,mp}$, one can enhance merger-driven BH growth by choosing a lower halo mass threshold $\tilde{M}_{\rm h}$; this would relax the constraints on the accretion model in producing $z \sim 6$ quasars.

Prospects for DCBH formation in the 5SIGMA_COMPACT region are limited if the critical LW fluxes are indeed $\gtrsim 1000\, J_{21}$ as predicted by one-zone chemistry models and small-scale hydrodynamics simulations. This is because LW intensities within the dense, metal-poor pockets of 5SIGMA_COMPACT region do not significantly exceed $\sim 300\, J_{21}$ between $z \sim 7$ and 22. 5SIGMA_COMPACT region produces a handful of seeds for somewhat lower critical fluxes, particularly $\sim 300\ J_{21}$. Even for these optimistic estimates of $J_{\rm crit}$, due to the obvious lack of merger-driven BH growth, DCBHs would require one of the optimal accretion scenarios described in the previous paragraph in order to grow a $z \gtrsim 6$ quasar. However, DCBHs could form even in the absence or lack of LW radiation under several scenarios described in the literature. These include suppression of H_2 induced by collisional dissociation or trapping of Lyman α by neutral Hydrogen (Spaans & Silk 2006; Schleicher et al. 2010; Latif et al. 2011; Inayoshi & Omukai 2012), supersonic gas streaming (Tanaka & Li 2014; Hirano et al. 2017; Schauer et al. 2019), and dynamical heating during rapid growth of massive haloes (Fernandez et al. 2014; Wise et al. 2019; Regan et al. 2020) (see also Section 1 for more details). Inclusion of these scenarios could lead to more seeds, resulting in better prospects for explaining the high-z quasars using the DCBH seeding channel. As far as other theoretical seeding channels such as Pop III and NSC seeds, without being able to explicitly resolve their formation conditions, it is currently difficult to tell whether they form and merge abundantly enough to qualify as potential origins of the $z \gtrsim 6$ quasars. We shall investigate all these seed formation channels in the future.

We note that our results are specific to features of our underlying IllustrisTNG galaxy formation model. They may significantly depend on the prescriptions for star formation, metal enrichment, stellar feedback, and BH dynamics. Additionally, there are also several other BH seeding, accretion, and feedback models beyond the ones explored in this work, that could potentially produce $z \sim 6$ quasars. BH accretion and feedback is a major source of uncertainty. For example, the lack of accretion-driven BH growth at $z \gtrsim 9$ may be partly influenced by the Bondi accretion model which struggles to grow low mass BHs due to the M_{bh}^2 scaling of the accretion rate. This M_{bh}^2 scaling also implies that at these early epochs when the self-regulation by feedback is relatively weak, the BH growth would be extremely sensitive to the local gas environment. This local gas environment may be impacted by other aspects of galaxy formation, such as star formation, stellar feedback (for e.g. Habouzit et al. 2017), metal enrichment, and gas cooling. While the M_{bh}^2 scaling appears as a generic feature of all accretion models based on a gas capture radius (Springel, Di Matteo & Hernquist 2005; Pelupessy, Di Matteo & Ciardi 2007; Booth & Schaye 2009), there are also models such as gravitational torque driven accretion (Anglés-Alcázar et al. 2017; Davé et al. 2019) where the scaling exponent is smaller ($M_{bh}^{1/6}$). This can significantly boost the growth of low-mass BHs, but also slow down the growth of high-mass BHs. As a result, it can have non-trivial implications for the feasibility of various BH models to produce $z \gtrsim 6$ quasars.

A final caveat to our results lies within our modelling of BH dynamics. In particular, due to the limited simulation resolution, we use the standard BH repositioning scheme which instantaneously relocates the BH to a nearby potential minimum. In fact, several simulations with more realistic dynamics models (e.g. Tremmel et al. 2017) have now indicated that it may be difficult for many of the seeds (particularly lower mass seeds) to sink to the local potential minima, thereby leading to a population of wandering BHs (Tremmel et al. (Tremmel et al. 2018; Ma et al. 2021; Ricarte et al. 2021a, b; Weller et al. 2022). This would have two important effects: (1) overestimating the accretion rates since the BHs may spend more time around dense gas compared to more realistic dynamics models, and (2) nearby BHs are promptly merged, thereby overestimating the merger rates at early times. In the future, we shall assess the impact of all of these caveats on the formation of $z \gtrsim 6$ quasars.

Despite the caveats, our results overall indicate a strong prospect of revealing the seeding environments for the observed $z \gtrsim 6$ quasars using upcoming facilities such as LISA. In particular, regardless of the accretion model, different seed models predict distinct merger and accretion histories for the progenitors of these quasars at $z \gtrsim 9$. These progenitors will also be amongst the most massive sources at their corresponding redshift. In addition to the strong prospect of detecting their mergers with LISA up to $z \sim 20$, their AGN luminosities also exceed detection limits of Lynx and *JWST* up to $z \sim 10$. However, the difference in the predicted AGN luminosities between different seed models is small ($\lesssim$2.5 dex in magnitude). Therefore, detecting electromagnetic signatures of seeding is going to be challenging for *JWST* and Lynx.

ACKNOWLEDGEMENTS

AKB thanks Dylan Nelson for valuable discussion and feedback. LB acknowledges support from NSF award AST-1909933 and Cottrell Scholar Award #27553 from the Research Corporation for Science Advancement. PT acknowledges support from NSF-AST 2008490. RW is supported by the Natural Sciences and Engineering Research Council of Canada (NSERC), funding reference #CITA 490888-16. TDM acknowledges funding from NSF AST-1616168, NASA ATP 80NSSC20K0519, NASA ATP 80NSSC18K101, and NASA ATP NNX17AK56G. This work was also supported by the NSF AI Institute: Physics of the Future, NSF PHY-2020295. YN acknowledges support from the McWilliams fellowship.

DATA AVAILABILITY

The underlying data used in this work shall be made available upon reasonable request to the corresponding author.

REFERENCES

Anglés-Alcázar D., Davé R., Faucher-Giguère C.-A., Özel F., Hopkins P. F., 2017, MNRAS, 464, 2840
Bañados E. et al., 2018, Nature, 553, 473
Bañados E. et al., 2016, ApJS, 227, 11

Baker J. et al., 2019, BAAS, 51, 77
Barausse E., 2012, MNRAS, 423, 2533
Barnes J., Hut P., 1986, Nature, 324, 446
Begelman M. C., Volonteri M., Rees M. J., 2006, MNRAS, 370, 289
Bellovary J., Volonteri M., Governato F., Shen S., Quinn T., Wadsley J., 2011, ApJ, 742, 13
Bhowmick A. K., Blecha L., Torrey P., Kelley L. Z., Vogelsberger M., Nelson D., Weinberger R., Hernquist L., 2021a, MNRAS, 510, 177
Bhowmick A. K. et al., 2021b, MNRAS, 507, 2012
Booth C. M., Schaye J., 2009, MNRAS, 398, 53
Bromm V., Loeb A., 2003, ApJ, 596, 34
Cann J. M., Satyapal S., Abel N. P., Ricci C., Secrest N. J., Blecha L., Gliozzi M., 2018, ApJ, 861, 142
Chabrier G., 2003, PASP, 115, 763
Chen N., Ni Y., Tremmel M., Di Matteo T., Bird S., DeGraf C., Feng Y., 2022, MNRAS, 510, 531
Costa T., Sijacki D., Trenti M., Haehnelt M. G., 2014, MNRAS, 439, 2146
Curtis M., Sijacki D., 2016, MNRAS, 457, L34
Das A., Schleicher D. R. G., Basu S., Boekholt T. C. N., 2021a, MNRAS, 505, 2186
Das A., Schleicher D. R. G., Leigh N. W. C., Boekholt T. C. N., 2021b, MNRAS, 503, 1051
Davé R., Anglés-Alcázar D., Narayanan D., Li Q., Rafieferantsoa M. H., Appleby S., 2019, MNRAS, 486, 2827
Davies M. B., Miller M. C., Bellovary J. M., 2011, ApJ, 740, L42
Dayal P., Rossi E. M., Shiralilou B., Piana O., Choudhury T. R., Volonteri M., 2019, MNRAS, 486, 2336
DeGraf C., Sijacki D., 2020, MNRAS, 491, 4973
Debuhr J., Quataert E., Ma C.-P., Hopkins P., 2010, MNRAS, 406, L55
Di Matteo T., Khandai N., DeGraf C., Feng Y., Croft R. A. C., Lopez J., Springel V., 2012, ApJ, 745, L29
Di Matteo T., Croft R. A. C., Feng Y., Waters D., Wilkins S., 2017, MNRAS, 467, 4243
Donnari M. et al., 2019, MNRAS, 485, 4817
Dubois Y., Pichon C., Devriendt J., Silk J., Haehnelt M., Kimm T., Slyz A., 2013, MNRAS, 428, 2885
Dubois Y., Peirani S., Pichon C., Devriendt J., Gavazzi R., Welker C., Volonteri M., 2016, MNRAS, 463, 3948
Elvis M. et al., 1994, ApJS, 95, 1
Fan X. et al., 2001, AJ, 122, 2833
Feng Y., Di Matteo T., Croft R., Khandai N., 2014, MNRAS, 440, 1865
Feng Y., Di-Matteo T., Croft R. A., Bird S., Battaglia N., Wilkins S., 2016, MNRAS, 455, 2778
Feng Y., Bird S., Anderson L., Font-Ribera A., Pedersen C., 2018, MP-Gadget/MP-Gadget: A tag for getting a DOI
Fernandez R., Bryan G. L., Haiman Z., Li M., 2014, MNRAS, 439, 3798
Fryer C. L., Woosley S. E., Heger A., 2001, ApJ, 550, 372
Gardner J. P. et al., 2006, Space Sci. Rev., 123, 485
Genel S. et al., 2018, MNRAS, 474, 3976
Habouzit M., Volonteri M., Dubois Y., 2017, MNRAS, 468, 3935
Habouzit M. et al., 2021, MNRAS, 503, 1940
Habouzit M. et al., 2022a, MNRAS, 511, 3751
Habouzit M. et al., 2022b, MNRAS, 509, 3015
Hirano S., Hosokawa T., Yoshida N., Umeda H., Omukai K., Chiaki G., Yorke H. W., 2014, ApJ, 781, 60
Hirano S., Hosokawa T., Yoshida N., Kuiper R., 2017, Science, 357, 1375
Hirschmann M., Dolag K., Saro A., Bachmann L., Borgani S., Burkert A., 2014, MNRAS, 442, 2304
Hoffman Y., Ribak E., 1991, ApJ, 380, L5
Hosokawa T., Hirano S., Kuiper R., Yorke H. W., Omukai K., Yoshida N., 2016, ApJ, 824, 119
Hu H., Inayoshi K., Haiman Z., Li W., Quataert E., Kuiper R., 2022, preprint (arXiv:2204.12513)
Huang K.-W., Ni Y., Feng Y., Di Matteo T., 2020, MNRAS, 496, 1
Inayoshi K., Omukai K., 2012, MNRAS, 422, 2539
Inayoshi K., Onoue M., Sugahara Y., Inoue A. K., Ho L. C., 2022, ApJ, 931, L25
Jiang L. et al., 2016, ApJ, 833, 222
Katz N., Weinberg D. H., Hernquist L., 1996, ApJS, 105, 19
Kaviraj S. et al., 2017, MNRAS, 467, 4739
Khandai N., Di Matteo T., Croft R., Wilkins S., Feng Y., Tucker E., DeGraf C., Liu M.-S., 2015, MNRAS, 450, 1349
Kroupa P., Subr L., Jerabkova T., Wang L., 2020, MNRAS, 498, 5652
Latif M. A., Zaroubi S., Spaans M., 2011, MNRAS, 411, 1659
Latif M. A., Schleicher D. R. G., Hartwig T., 2016, MNRAS, 458, 233
Latif M. A., Whalen D. J., Khochfar S., Herrington N. P., Woods T. E., 2022, Nature, 607, 48
Lee J. et al., 2021, ApJ, 908, 11
Li Y. et al., 2007, ApJ, 665, 187
Li W., Inayoshi K., Qiu Y., 2021, ApJ, 917, 60
Luo Y., Ardaneh K., Shlosman I., Nagamine K., Wise J. H., Begelman M. C., 2018, MNRAS, 476, 3523
Luo Y., Shlosman I., Nagamine K., Fang T., 2020, MNRAS, 492, 4917
Lupi A., Colpi M., Devecchi B., Galanti G., Volonteri M., 2014, MNRAS, 442, 3616
Lupi A., Volonteri M., Decarli R., Bovino S., Silk J., Bergeron J., 2019, MNRAS, 488, 4004
Lupi A., Haiman Z., Volonteri M., 2021, MNRAS, 503, 5046
Ma L., Hopkins P. F., Ma X., Anglés-Alcázar D., Faucher-Giguère C.-A., Kelley L. Z., 2021, MNRAS, 508, 1973
Madau P., Rees M. J., 2001, ApJ, 551, L27
Marinacci F. et al., 2018, MNRAS, 480, 5113
Matsuoka Y. et al., 2018, ApJS, 237, 5
Matsuoka Y. et al., 2019, ApJ, 872, L2
Mortlock D. J. et al., 2011, Nature, 474, 616
Naiman J. P. et al., 2018, MNRAS, 477, 1206
Natarajan P., Pacucci F., Ferrara A., Agarwal B., Ricarte A., Zackrisson E., Cappelluti N., 2017, ApJ, 838, 117
Nelson D. et al., 2018, MNRAS, 475, 624
Nelson D. et al., 2019, Comput. Astrophys. Cosmol., 6, 2
Ni Y., Matteo T. D., Feng Y., 2021, MNRAS, 509, 3043
Ni Y. et al., 2022, MNRAS, 513, 670
Pakmor R., Bauer A., Springel V., 2011, MNRAS, 418, 1392
Pakmor R., Pfrommer C., Simpson C. M., Kannan R., Springel V., 2016, MNRAS, 462, 2603
Pelupessy F. I., Di Matteo T., Ciardi B., 2007, ApJ, 665, 107
Pezzulli E., Valiante R., Schneider R., 2016, MNRAS, 458, 3047
Pezzulli E., Volonteri M., Schneider R., Valiante R., 2017, MNRAS, 471, 589
Pillepich A. et al., 2018a, MNRAS, 473, 4077
Pillepich A. et al., 2018b, MNRAS, 475, 648
Pillepich A. et al., 2019, MNRAS, 490, 3196
Planck Collaboration XIII, 2016, A&A, 594, A13
Reed S. L. et al., 2017, MNRAS, 468, 4702
Regan J. A., Johansson P. H., Wise J. H., 2014, ApJ, 795, 137
Regan J. A., Visbal E., Wise J. H., Haiman Z., Johansson P. H., Bryan G. L., 2017, Nat. Astron., 1, 0075
Regan J. A., Wise J. H., Woods T. E., Downes T. P., O'Shea B. W., Norman M. L., 2020, Open J. Astrophys., 3, 15
Ricarte A., Natarajan P., 2018, MNRAS, 481, 3278
Ricarte A., Tremmel M., Natarajan P., Zimmer C., Quinn T., 2021a, MNRAS, 503, 6098
Ricarte A., Tremmel M., Natarajan P., Quinn T., 2021b, ApJ, 916, L18
Rodriguez-Gomez V. et al., 2019, MNRAS, 483, 4140
Sassano F., Schneider R., Valiante R., Inayoshi K., Chon S., Omukai K., Mayer L., Capelo P. R., 2021, MNRAS, 506, 613
Schauer A. T. P., Glover S. C. O., Klessen R. S., Ceverino D., 2019, MNRAS, 484, 3510
Schaye J. et al., 2015, MNRAS, 446, 521
Schleicher D. R. G., Spaans M., Glover S. C. O., 2010, ApJ, 712, L69
Sesana A., Volonteri M., Haardt F., 2007, MNRAS, 377, 1711
Shang C., Bryan G. L., Haiman Z., 2010, MNRAS, 402, 1249
Sijacki D., Springel V., Haehnelt M. G., 2009, MNRAS, 400, 100
Sijacki D., Vogelsberger M., Genel S., Springel V., Torrey P., Snyder G. F., Nelson D., Hernquist L., 2015, MNRAS, 452, 575
Smidt J., Whalen D. J., Johnson J. L., Surace M., Li H., 2018, ApJ, 865, 126

Smith B., Sigurdsson S., Abel T., 2008, MNRAS, 385, 1443
Smith B. D., Regan J. A., Downes T. P., Norman M. L., O'Shea B. W., Wise J. H., 2018, MNRAS, 480, 3762
Spaans M., Silk J., 2006, ApJ, 652, 902
Springel V., 2010, MNRAS, 401, 791
Springel V., Hernquist L., 2003, MNRAS, 339, 289
Springel V., Di Matteo T., Hernquist L., 2005, MNRAS, 361, 776
Springel V. et al., 2018, MNRAS, 475, 676
Sugimura K., Omukai K., Inoue A. K., 2014, MNRAS, 445, 544
Tanaka T. L., Li M., 2014, MNRAS, 439, 1092
Taylor P., Kobayashi C., 2015, MNRAS, 448, 1835
Tenneti A., Wilkins S. M., Di Matteo T., Croft R. A. C., Feng Y., 2019, MNRAS, 483, 1388
The Lynx Team, 2018, preprint (arXiv:1809.09642)
Torrey P. et al., 2019, MNRAS, 484, 5587
Trebitsch M. et al., 2021, A&A, 653, A154
Tremmel M., Karcher M., Governato F., Volonteri M., Quinn T. R., Pontzen A., Anderson L., Bellovary J., 2017, MNRAS, 470, 1121
Tremmel M., Governato F., Volonteri M., Pontzen A., Quinn T. R., 2018, ApJ, 857, L22
Übler H. et al., 2021, MNRAS, 500, 4597
Valentini M., Gallerani S., Ferrara A., 2021, MNRAS, 507, 1
Valiante R., Schneider R., Salvadori S., Bianchi S., 2011, MNRAS, 416, 1916
Valiante R., Schneider R., Maiolino R., Salvadori S., Bianchi S., 2012, MNRAS, 427, L60
Valiante R., Schneider R., Salvadori S., Gallerani S., 2014, MNRAS, 444, 2442
Valiante R., Schneider R., Volonteri M., Omukai K., 2016, MNRAS, 457, 3356
Valiante R., Schneider R., Zappacosta L., Graziani L., Pezzulli E., Volonteri M., 2018, MNRAS, 476, 407
Vasudevan R. V., Fabian A. C., 2007, MNRAS, 381, 1235
van de Weygaert R., Bertschinger E., 1996, MNRAS, 281, 84
Venemans B. P. et al., 2015, MNRAS, 453, 2259
Visbal E., Haiman Z., Bryan G. L., 2014, MNRAS, 445, 1056
Vogelsberger M., Genel S., Sijacki D., Torrey P., Springel V., Hernquist L., 2013, MNRAS, 436, 3031
Vogelsberger M. et al., 2014a, MNRAS, 444, 1518
Vogelsberger M. et al., 2014b, Nature, 509, 177
Vogelsberger M., Marinacci F., Torrey P., Puchwein E., 2020a, Nat. Rev. Phys., 2, 42
Vogelsberger M. et al., 2020b, MNRAS, 492, 5167
Volonteri M., Natarajan P., 2009, MNRAS, 400, 1911
Volonteri M., Dubois Y., Pichon C., Devriendt J., 2016, MNRAS, 460, 2979
Volonteri M. et al., 2020, MNRAS, 498, 2219
Wang F. et al., 2018, ApJ, 869, L9
Wang F. et al., 2021, ApJ, 907, L1
Weinberger R. et al., 2017, MNRAS, 465, 3291
Weinberger R. et al., 2018, MNRAS, 479, 4056
Weinberger R., Springel V., Pakmor R., 2020, ApJS, 248, 32
Weller E. J., Pacucci F., Hernquist L., Bose S., 2022, MNRAS, 511, 2229
Willott C. J. et al., 2010, AJ, 139, 906
Wise J. H., Regan J. A., O'Shea B. W., Norman M. L., Downes T. P., Xu H., 2019, Nature, 566, 85
Wolcott-Green J., Haiman Z., Bryan G. L., 2017, MNRAS, 469, 3329
Xu H., Wise J. H., Norman M. L., 2013, ApJ, 773, 83
Yang J. et al., 2019, AJ, 157, 236
Zhu Q., Li Y., Li Y., Maji M., Yajima H., Schneider R., Hernquist L., 2020, preprint (arXiv:2012.01458)

This paper has been typeset from a TEX/LATEX file prepared by the author.